AD-A125 698 EFFECT OF THE TEST ENVIRONMENT ON CREEP CRACK GROWTH RATES FOR NICKEL BAS..(U) MASSACHUSETTS INST OF TECH CAMBRIDGE DEPT OF MATERIALS SCIENC.. 1/1

UNCLASSIFIED R M PELLOUX ET AL. FEB 83 AFOSR-TR-83-0107 F/G 11/6 NL

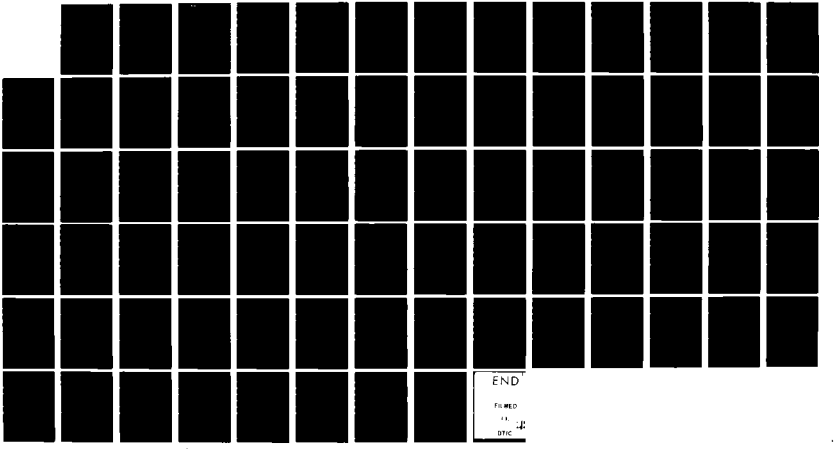

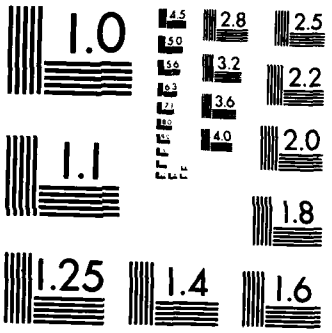

MICROCOPY RESOLUTION TEST CHART
NATIONAL BUREAU OF STANDARDS-1963 A

AFOSR-TR- 83-0107

AD A125698

ANNUAL REPORT

to

AIR FORCE OFFICE OF SCIENTIFIC RESEARCH

Project Manager: Dr. A. H. Rosenstein

Part I

EFFECT OF THE TEST ENVIRONMENT ON CREEP CRACK GROWTH RATES FOR NICKEL BASE ALLOYS

Part II

A STUDY OF CREEP CRACK GROWTH IN 2219-T851 ALUMINUM ALLOY USING A COMPUTERIZED TESTING SYSTEM

Approved for public release; distribution unlimited.

DTIC FILE COPY

Principal Investigator:

Regis M. Pelloux
Department of Materials Science and Engineering
Massachusetts Institute of Technology
Cambridge, Massachusetts 02139

DTIC ELECTE MAR 16 1983 D

83 03 14 130

SECURITY CLASSIFICATION OF THIS PAGE (When Data Entered)

UNCLASSIFIED

REPORT DOCUMENTATION PAGE	READ INSTRUCTIONS BEFORE COMPLETING FORM
1. REPORT NUMBER: AFOSR-TR- 83-0107	2. GOVT ACCESSION NO.: AD-A125698
	3. RECIPIENT'S CATALOG NUMBER
4. TITLE (and Subtitle): I. EFFECT OF THE TEST ENVIRONMENT ON CREEP CRACK GROWTH RATES FOR NICKEL BASE ALLOYS II. A STUDY OF CREEP CRACK GROWTH IN 2219-T851 ALUMINUM ALLOY USING A COMPUTERIZED TESTING SYSTEM.	5. TYPE OF REPORT & PERIOD COVERED: ANNUAL
	6. PERFORMING ORG. REPORT NUMBER
7. AUTHOR(s): Regis M. Pelloux, Kenneth R. Bain, Philippe L. Bensussan	8. CONTRACT OR GRANT NUMBER(s): AFOSR 82-0087
9. PERFORMING ORGANIZATION NAME AND ADDRESS: Massachusetts Institute of Technology, Cambridge, MA 02139	10. PROGRAM ELEMENT, PROJECT, TASK AREA & WORK UNIT NUMBERS: 61102F 2306/A1
11. CONTROLLING OFFICE NAME AND ADDRESS: Air Force Office of Scientific Research, Bolling Air Force Base, DC 20332	12. REPORT DATE: Feb. 1983
	13. NUMBER OF PAGES: 69
14. MONITORING AGENCY NAME & ADDRESS (if different from Controlling Office)	15. SECURITY CLASS. (of this report): unclassified
	15a. DECLASSIFICATION/DOWNGRADING SCHEDULE

16. DISTRIBUTION STATEMENT (of this Report)

Approved for public release; distribution unlimited.

17. DISTRIBUTION STATEMENT (of the abstract entered in Block 20, if different from Report)

18. SUPPLEMENTARY NOTES

DTIC COPY INSPECTED 2

Accession For
NTIS GRA&I [X]
DTIC TAB [ ]
Unannounced [ ]
Justification
By
Distribution/
Availability Codes
Dist | Avail and/or Special
A

19. KEY WORDS (Continue on reverse side if necessary and identify by block number)

creep crack growth rate, nickel base superalloys, high strength aluminum alloys, automated testing procedures, fracture mechanics, environmental effects.

20. ABSTRACT (Continue on reverse side if necessary and identify by block number)

A two part research program was conducted to study the mechanics of creep crack growth in 1) nickel base superalloys as a function of alloy chemistry and test environment at 704°C; 2) a high strength aluminum alloy 2219-T851 at 175°C. The creep crack growth rate data is reported and analyzed in terms of fracture mechanics parameters. The automated test procedures used for the aluminum alloys is discussed in detail in view of the need for standardized testing procedures to measure creep crack growth rates.

DD FORM 1 JAN 73 1473 EDITION OF 1 NOV 65 IS OBSOLETE

UNCLASSIFIED

SECURITY CLASSIFICATION OF THIS PAGE (When Data Entered)

PART I

EFFECT OF THE TEST ENVIRONMENT ON CREEP CRACK GROWTH RATES FOR NICKEL BASE ALLOYS

Kenneth R. Bain
Graduate Student

ABSTRACT

The creep crack growth rates (CCGR) for PM/HIP low carbon Astroloy, Merl-76, low carbon IN-100, and René-95 were determined in air and in 99.999% pure argon at 704°C. The tests ranged from K = 10 to 150 MPa$\sqrt{m}$ and from da/dt = 10^{-9} m/s to 10^{-3} m/s. Single edge notched specimens with and without fatigue precracking were used in CCGR tests. The crack length was determined via d.c. electrical potential drop. Environment was found to have a varying effect on different alloys, but air was found to increase the da/dt by up to 100 times over argon, and a reduced threshold for CCG was suggested.

The fracture path was intergranular in all CCGR tests. A transition from intergranular cracking in air to a prior particle boundary fracture path in argon CCGR tests was observed in all alloys.

Tensile, creep, creep-rupture, and notched stress-rupture (NSR) tests were performed at 704°C in air. The constitutive relationships for strain hardening and secondary creep rate were determined for each alloy. The NSR tests indicate that the relative time to rupture of each alloy correlates with that alloy's ability to resist CCG in air.

Part I

EFFECT OF THE TEST ENVIRONMENT ON CREEP CRACK GROWTH RATES FOR NICKEL BASE ALLOYS

TABLE OF CONTENTS

Abstract. i

1. Introduction. 1

2. Experimental Procedures 2

2.1 Material. 2

2.2 Microstructural Characterization. 3

2.3 Mechanical Testing. 3

2.3.1. Tensile Testing. 4

2.3.2. Smooth Bar Creep Testing 4

2.3.3. Notched Stress Rupture Testing 4

2.3.4. Creep Crack Growth Rate Testing. 4

3. Experimental Results. 5

3.1. Tensile Tests. 5

3.2. Creep Rate Tests 6

3.3. Notched Stress Rupture Results 6

3.4. Creep Crack Growth Results 7

3.5. Fractography 8

4. Discussion. 8

5. Future Research 9

References. 10

Tables. 11

Figures 13

EFFECT OF ENVIRONMENT ON CREEP CRACK GROWTH RATES FOR NI BASE ALLOYS

1. INTRODUCTION

Creep crack growth is a process in which a crack advances intergranularly in a material with a constant tensile stress at temperatures where creep deformation is possible. ($T > .5\ T_m$; T_m = melting point). In an inert test environment the micromechanism of creep crack advance consists of nucleation, growth, and coalescence of grain boundary cavities [1, 2, 3]. While attempts to model this behavior have been presented by several researchers [8-13], none has shown the ability to predict creep crack growth reliably in nickel base superalloys, and environment is not taken into account.

Tests comparing CCGR for several nickel base alloys show up to a 1000 time increase in da/dt for tests in air over those in an inert environment [1, 14, 15]. Research on creep-rupture properties has shown that oxygen [16] and carbon dioxide [17] sharply reduce fracture ductility and time to rupture in nickel base alloys. CCG tests in environments containing SO_2 show an increase in crack growth which is greater than in air or oxygen [10]. CCGR behavior for nickel base alloys in air varies considerably, while in an inert environment the range of results is greatly reduced. This indicates that the ability of an alloy to resist embrittlement in an aggressive environment greatly influences the CCGR of that alloy. The chemistry at the grain boundaries in nickel base alloys and elements which segregate there such as B, Zr, and C can be expected to affect the behavior of an alloy. Grain size, particle size and particle distribution will also influence the CCG process in all environments [2].

Overaging and coarsening of γ' in nickel base alloys has also been suggested to reduce CCGR by promoting wavy slip in the matrix, which reduces local formation of cavities on grain boundaries [3]. In many ways CCG in an aggressive environment causes behavior very similar to the stress corrosion cracking phenomenon observed at lower temperatures.

Several mechanisms have been proposed to explain this acceleration in CCGR. They include diffusion of O_2 into grain boundaries ahead of

the crack tip and subsequent formation of carbon monoxide bubbles at carbides. This mechanism is similar to the formation of methane bubbles proposed to explain the effect of hydrogen in steels. The formation of complex oxides can act as nucleation sites for cavities. A reaction of oxygen with MnS particles will release free sulfur to the grain boundaries, and thus lower the interfacial strength of grain boundary carbides which would allow nucleation of crack-like cavities. While all these mechanisms are possible, none has been conclusively proven.

The following research is being performed to investigate the effect of test procedures, alloy, and environment on CCGR in nickel base alloys.

2. EXPERIMENTAL PROCEDURES

2.1 Material

Four γ/γ' nickel base superalloys were chosen for this study. They are Low Carbon Astroloy, Merl-76, Low Carbon IN-100, and René-95. The alloys were produced by HIP processing of PM alloys into 9/16" diameter rod. These alloys were chosen for study as a result of the varying susceptibility to grain boundary embrittlement in oxygen. The powder mesh size for each alloy is shown in Table 1, along with the particle diameter. René-95 was obtained in two mesh sizes.

Table I
Powder Size

	Mesh	Particle diameter, μm
Astroloy	100	149
Merl-76	325	45
IN-100	60	250
René-95	60	250
René-95	120	125

Table II describes the thermal and HIP processing given to the alloys used in this study. The heat treatment was chosen to give the alloys similar mechanical properties.

TABLE II
Thermal Processing

1. HIP Cycle
   a. Astroloy - 1232°C/4 hours/Furnace cool/15 Ksi
   b. IN-100, Merl-76, René-95 - 1177°C/4 hours/ Furnace Cool/15 Ksi
2. Heat Treatment
   Solution: 1177°C/4 hours/air cool
   Age: 871°C/8 hours/air cool
   982°C/4 hours/air cool
   650°C/24 hours/air cool
   760°C/8 hours/air cool

The chemistries for the alloys are shown in Table III. The calculated γ' volume fraction for each alloy is also given in Table III. [4]. Trace elements which segregate to the grain boundaries such as B, Zr, C, O, P and S were determined.

2.2 Microstructural Characterization

Several samples of heat treated material were mounted in Buehler plastimet, ground on 240, 320, 400, and 600 grit silicon carbide paper, then ground with three μm paste on nylon cloth and finally polished with Nalcoag 1060 (colloidal silica solution) on nylon cloth. The specimens were etched using No. 2 stainless reagent (100 ml methanol, 50 ml HCl, and 5 gm $FeCl_3$).

The etched specimens were observed under both a Zeiss Universal optical microscope and an AMR-1000 A scanning electron microscope. Figures 1-4 show the after heat treatment microstructures of Astroloy, Merl-76, IN-100, and René-95 respectively. IN-100 and Astroloy have coarse grain size with carbides decorating the grain boundaries. Merl-76 and René-95 have a finer grain size with large primary γ' particles along the boundaries.

2.3 Mechanical Testing

Tensile, creep, creep rupture, notched stress rupture, and creep

crack growth tests were performed at 704°C on all four alloys. The test procedures for these tests are described in the following sections.

2.3.1 Tensile Testing

Testing was performed using an Instron Tensile Machine. The test was performed at 704°C at a displacement rate of .02 inches per minute. An A.T.S. three-zone resistance heater with a Leeds and Northrup Electromax III temperature controller was used for heating the specimen. Load versus displacement was recorded using a strip chart recorder incorporated in the Instron machine. A yield stress of .2 per cent and ultimate tensile strength was determined graphically. Total elongation and reduction of area was measured directly on the failed bar.

2.3.2 Smooth Bar Creep Testing

Tests were conducted to obtain the minimum creep rate versus stress at 704°C. Creep rate tests were conducted at 704°C within the stress range from 650 to 1050 MPa. Temperature control was accurate to within ±4°C within the specimen gauge section. The elongation was measured using an extensometer corrected to a dc-dc LVDT with a .25 inch range from 0 to 100 mV. Tests were conducted using an A.T.S. level arm tester. The steady state creep rate was recorded at each stress level. The stress was increased in steps in order to obtain several stress and steady state creep rate points per specimen. Several smooth bars were tested at one stress and the time to rupture was recorded along with the minimum creep rate.

2.3.3 Notched Stress Rupture Testing

The specimen geometry is shown in Figure 5. The stress concentration factor K_t = 3 with 60° flank angles, and root radius .013 inch. Tests were conducted at 704°C in air using the same A.T.S. level arm testing system and temperature control as in Section 2.3.2. Only time to rupture was recorded at various stress levels.

2.3.4 Creep Crack Growth Rate Testing

Creep crack growth rate tests were conducted at constant load using a level arm tester supplied by Applied Testing System Company (ATS). Temperature was controlled within ±4°C within the gauge section of the specimen using a 3-zone resistance heater. Tests were

conducted in two environments: in air and in an inert environment of 99.999 percent pure argon. A retort supplied by ATS was used in the argon tests. Argon tests were conducted at a pressure of 5 psig in order to insure no back streaming of air.

A single edge-notched test specimen is used in the creep crack growth rate tests. (Figure 6). This specimen has side grooves to prevent crack tip tunnelling as a result of the slower creep crack growth rate in the plane stress condition which would otherwise exist on the specimen surface.

A starter notch is cut using a 150 μm thick diamond saw. Specimens were fatigue precracked at room temperature. The maximum stress intensity, K, used in precracking is less than the initial stress intensity used in subsequent creep crack growth testing. Crack length is measured using the d.c. electrical potential technique (5,6). The short crack length and large range of crack length/width ratio afforded by the SEN specimen geometry gives a resolution of 10 μm change in crack length. A 30 amp constant d.c. current is passed through the specimen and the potential across the crack mouth versus time is recorded.

Each specimen is individually calibrated using the initial and final crack lengths and d.c. potentials. This removes the variation in crack length determination as a result of the uncertainty in the potential probe spacing, Y. The theoretical solution by Johnson (7) was used to calibrate the crack length time from the d.c. potential:

$$\frac{V_a}{V_{a_o}} = \frac{\cosh^{-1}\left[\frac{\cosh(\pi Y/2W)}{\cos(\pi a/2W)}\right]}{\cos^{-1}\left[\frac{\cosh(\pi Y/2W)}{\cos(\pi a_o/2W)}\right]}$$

where V_{a_o} is the initial potential across the crack mouth, Y is one-half the potential load spacing, W is the specimen width, and a_o is the initial crack length.

3. Experimental Results

3.1 Tensile Tests

A tensile test at 704°C was conducted for each alloy. The tensile test results are shown in Table IV. The U.T.S., .2% Y.S., and

Elastic Modulus for all the alloys are approximately the same. The percentage elongation varies by a factor of three from 5.0% for René-95 to 15.4% for Astroloy. The specimens with low ductility exhibited failure by the propagation of surface cracks. The plastic strain hardening exponent N_p and proportionality constant B_p are also given in Table IV ($\sigma = B_p(\varepsilon_p)^{N_p}$).

3.2 Creep Rate Tests

The steady state creep rate for each alloy was measured in air at 704°C for a range of applied stresses from 600 to 1100 MPa. The results are shown in Figure 7 in a plot of stress versus steady state creep rate. The exponent and constant from the secondary creep rate equation are also shown. (σ(MPa) = $N_c(\dot{\varepsilon}_s)^{N_c}$). In the range of steady state creep rate from 10^{-8} sec^{-1} to $10^{-Y}sec^{-1}$. The behavior of the four alloys is the same. Only René-95 exhibits a slight increase in the creep exponent.

Four tests (one from each alloy) were stressed to 801 MPa in air at 704°C and run to failure. The results showed the four alloys to be very similar with the exception of Merl-76 which had a slightly longer time to rupture. The individual results are shown below:

Table V
Creep-Rupture Results, Air, 704°C, 801 MPa

	t_f(hrs)
René-95	7.2
IN-100	4.7
Merl-76	28.7
Astroloy	5.8

3.3 Notched Stress Rupture Results

Notched stress rupture tests were performed on all four alloys in air at 704°C. The results are shown in Figure 8. The results show that the René-95 rupture time is much shorter than the other three alloys tested. At high stress Merl-76 gives the longest time to rupture, but at the lower stress a crossover occurs and Astroloy has a longer time to rupture.

Several René-95 specimens were pre-exposed to air at 704°C with either a low applied load or no load and failed at a high load. The results are summarized in Table VI.

TABLE VI

Notched Stress-Rupture of René-95, 704°C

Pre-exposure	Test Results
408 MPa/403.4 hrs	675 MPA/<1 min.
No Pre-exposure	591 MPa/ 137.2 hrs.
0 MPa/73.4 hrs.	591 MPa/237.8 hrs.
338 MPa/69.0 hrs.	571 MPa/153.8 hrs.

The tests were inconclusive but they did present a few interesting results. Pre-exposure in air with a small tensile stress was more damaging than a pre-exposure to air with no stress, and a long pre-exposure with a small stress exhausted the residual life at the higher load.

3.4 Creep Crack Growth Results

Creep crack growth tests were performed in air and 9.999% pure argon on all four alloys. The creep crack growth rates at 704°C for PM/HIP low carbon Astroloy, Merl-76, IN-100, René-95 (60 mesh size) and René-95 (120 mesh size) are shown in Figures 9 through 14 respectively.

The inert environment tests were repeated for Merl-76, IN-100, and Astroloy and the results indicated that the stress intensity factor, K, does correlate with the creep crack growth rate. A threshold for creep crack growth rate in argon was not observed. The lowest K value used in each test is determined by the maximum K used in the room temperature fatigue pre-cracking of the individual specimen. All argon test specimens were fatigue pre-cracked. In the linearly increasing region of creep crack growth behavior the exponent on K is 4.2 for IN-100, René-95 (both 60 and 120 mesh), and Merl-76; and 9.5 for Astroloy. Figure 15 shows all the argon CCGR results for all alloys tested. The

scatter is two orders of magnitude in da/dt with PM/HIP René-95 having the fastest CCGR and Merl-76 having the lowest CCGR.

The CCGR results in air at 704°C for all the tests with a gross section stress away from the crack of ≈ 150 MPa is shown in Figure 16. The observed creep crack growth rate increases quickly until a region of linear crack growth rate increase is reached. When the initial stress intensity is high the crack will grow to K_{IC} before the region of linearly increasing crack growth is reached. The exponent on K in the linearly increasing region varies from 0.5 for René-95 (60 and 120 mesh size), and Merl-76 to 3.0 for IN-100 and Astroloy. The CCGR in air is increased up to 100 times over the CCGR in argon for all the alloys tested but Astroloy, which was not affected. The stress intensity factor does correlate CCGR's in Merl-76, IN-100 and René-95, but Astroloy tests show an increase in the CCGR at a given K as the applied gross section stress increases. The measured threshold for CCG in air is a function of the initial K applied as was observed in the argon tests. The increase in da/dt and decrease in the exponent on K suggest a lowering of the threshold value for CCGR if one does exist.

3.5 Fractography

Fracture surfaces were observed for both air and argon CCGR tests using an AMR-1000 Scanning Electron Microscope. The fracture path was intergranular for all CCGR tests. In the argon CCGR tests the crack followed prior powder particle boundaries. The prior particle boundaries in PM/HIP alloys are heavily decorated with carbides. Figure 17 shows a typical fracture surface for Astroloy in argon, and the round powder particles can be clearly seen. In air, the fracture path follows both prior powder particle boundaries and grain boundaries which cut through the particles. This is shown in Figure 18 for Astroloy. The creep crack in air tests follows the closest grain boundary normal to the applied stress.

4. DISCUSSION

The effect of oxygen on creep crack growth is significant. The CCGR behavior in air strongly resembles the behavior of steels during stress corrosion cracking (SCC). There is an initial transient and there probably is a K_{ISCC} below which creep crack growth in air will not occur, but this parameter is difficult to determine. This region is

at high stress, the reverse is true. The CCGR for Astroloy in air is lower than Merl-76 at low K, but Merl-76 and Astroloy are the same at high K. The NSR test is a valuable, fast, and simple test to evaluate the relative CCGR properties of nickel base alloys.

5. FUTURE RESEARCH

Additional research will be performed to understand the creep crack growth process in air. These include:

1. Development of an iterative-computer model which takes into account environmental embrittlement as well as nucleation, growth and coalescence of grain boundary cavities as micromechanisms controlling the crack advance.

2. Additional CCGR testing in air on Astroloy to investigate the effect of stress on the creep crack growth rate.

3. Combined fatigue-hold time tests will be performed to evaluate the depth of oxygen penetration along grain boundaries in air at 704°C. These tests will allow a calculation of an effective diffusion coefficient for each alloy to be used in the development of a model.

4. Detailed fractography of fracture surfaces in tests performed in air and in argon.

followed by a region of K-insensitive crack growth. This region of K-insensitive growth has been explained as a region where a transport mechanism is rate-limiting. This transport mechanism can be transport of oxygen to the crack tip, adsorption of the oxygen in the crack tip, absorption of oxygen into the material, and finally diffusion of oxygen ahead of the crack tip (19). The region of K-insensitive crack growth is followed by a region where the crack growth rate increases quickly until final fast fracture at K_{IC}.

The tensile and smooth bar creep results on the alloys do not indicate any trends which might help to explain the behavior observed in creep crack growth. The alloy microstructure and chemistry indicate that alloys high in boron such as Astroloy and low in carbon exhibit low creep crack growth rates.

The CCGR behavior of Astroloy in air indicates that when the environment is active at the crack tip, the stress intensity factor alone is not enough to predict the creep crack growth rates for an alloy. This should be expected since K does not take into account any time-dependent diffusion mechanisms, but only characterizes the state of stress at the crack tip. A parameter which takes into consideration these time-dependent changes in the material at the tip of a crack remains to be developed. The creep crack growth rate under these conditions may only be characterized by iterative computer modelling of the processes which are occurring.

The relative behavior in CCGR tests between the alloys tested in air can be predicted by examination of notched stress rupture (NSR) results in air. The conditions of the notch test simulate the high stress and localized plasticity that are experienced at a crack tip. The micromechanisms which control the creep crack growth process at the tip of the crack are expected to operate at the root of the notch and control the time to rupture in the NSR specimen. Therefore, NSR results can provide information useful in evaluating an alloy's susceptibility to creep crack growth. René-95 gives the shortest times to rupture and also exhibits the highest CCGR in air. (Figure 16.) Astroloy has a longer time to rupture than Merl-76 at low stress, but

References

1. R. M. Pelloux and J. S. Huang, Creep-Fatigue-Environment Interactions, Proceedings AIME, ed. by R. M. Pelloux and N. S. Stoloff, p. 151, 1980.

2. S. Floreen, ibid, p. 112.

3. C. H. Wells, Fatigue and Microstructure, ASM conference proceedings, October 1978, p. 307.

4. O. H. Kriege and J. M. Baris, Trans. ASM 62, p. 195, 1969.

5. R. O. Ritchie, "Crack Growth Monitoring: Some Considerations on the Electrical Potential Method", University of Cambridge, 1972.

6. M. D. Halliday and C. J. Beevers, The Measurement of Crack Length and Shape during Fracture and Fatigue, 1980, p. 85.

7. H. H. Johnson, Materials Research and Standards, Vol. 5, 1965, p. 442.

8. V. Vitek, Acta Met., 26, 1978, p. 1345.

9. R. Pilkington and D. Miller, Met. Trans. A., 11A, 1980, p. 177.

10. R. Raj and S. Baik, "Creep Crack Growth by Cavitation near Crack Tip", to be published in Metal. Sci.

11. R. Pilkington, D. A. Miller and D. Worswick, Met. Trans. A., 12A, February 1980, p. 173.

12. J. T. Barnby, Eng. Fracture Mech., Vol 7., 1975, p. 299.

13. W. D. Nix, D. Matlock and R. Dimelfi, Acta Metal., Vol. 25, 1977, p. 495.

14. F. Gabrielli and R. M. Pelloux, Met. Trans. A., 13A, 1982, p. 1083.

15. K. Sadananda and P. Shahinian, Creep-Fatigue-Environment Interactions, Proceedings AIME, ed. by R. M. Pelloux and N. S. Stoloff, 1980, p. 86.

16. R. H. Bricknell and D. A. Woodford, Creep and Fracture of Engineering Materials and Structures, ed. by B. Wilshin and D. R. Owen, Proceedings, Int. Conf. University College, Swansea, March 1981.

17. R. C. Cobb, Materials Science and Engineering, 38 (1979), p. 249-258.

18. S. Floreen, "Symposium on Fracture Mechanics", Proceedings, ASTM Conf, October 1981.

19. H. L. Marcus, Fatigue and Microstructure, Proceedings, ASM conference, October 1978, p. 365.

TABLE III

Alloy Chemistries

	Sample 1 Astroloy %	Sample 2 Rene-95 %	Sample 3 Merl-76 %	Sample 4 IN-100 %
Chromium	14.8	14.0	12.2	12.2
Cobalt	16.3	7.71	17.8	18.3
Molybdenum	4.82	3.33	3.20	3.39
Columbium	.004	3.36	1.36	<.001
Aluminum	3.97	3.31	4.71	4.88
Titanium	3.39	2.41	4.19	4.17
Hafnium	.01	.01	.10	<.01
Vanadium	<.001	.007	.009	.97
Carbon	.044	.082	.034	.082
Boron	.025	.007	.020	.021
Zirconium	.037	.064	.050	.037
Oxygen	.0129	.0137	.0238	.0111
Sulfur	<.001	.001	<.001	<.001
Phosphorus	.014	<.001	<.001	<.001
Nitrogen	.0008	.0020	.0029	.0016
Silicon	.02	.07	.10	.04
Iron	.24	.18	.077	.082
Tungsten		3.42		
Nickel	Remainder	Remainder	Remainder	Remainde
γ' Volume Fraction (Calculated)	0.46	0.38	0.58	0.63

TABLE IV

704°C Tensile Test Results

	U.T.S. (MPa)	.2% Y.S. (MPa)	% El.	E (GPa)	Bp (MPa)	Np
René-95	1199	947	5.0	167	1083	.099
IN-100	1167	1012	8.4	162	1103	.058
MERL-76	1164	1012	13.1	160	1103	.056
Astroloy	1200	950	15.4	170	1055	.088

LIST OF FIGURES

Figure 1. Photomicrograph of PM/HIP low carbon Astroloy (500 X).

Figure 2. Photomicrograph of PM/HIP MERL-76 (500 X).

Figure 3. Photomicrograph of PM/HIP low carbon IN-100 (500X).

Figure 4. Photomicrograph of PM/HIP Rene-95 (500 X).

Figure 5. Notched stress rupture specimen geometry. K_t = 3.18.

Figure 6. Single edge notched specimen geometry with side grooves.

Figure 7. Plot of stress versus secondary creep rate for Astroloy, MERL-76, IN-100, and Rene-95 at 704°C in air.

Figure 8. Plot of NSR results in air at 704°C shown as stress versus time to rupture.

Figure 9. CCGR versus K for PM/HIP low carbon Astroloy in air and argon at 704°C.

Figure 10. CCGR versus K for PM/HIP MERL-76 in air and argon at 704°C.

Figure 11. CCGR versus K for PM/HIP low carbon IN-100 in air and argon at 704°C.

Figure 12. CCGR versus K for PM/HIP Rene-95 (60 mesh) in air and argon at 704°C.

Figure 13. CCGR versus K for PM/HIP Rene-95 (120 mesh) in air and argon at 704°C.

Figure 14. CCGR versus K for all four Nickel-base alloys in argon at 704°C.

Figure 15. CCGR versus K for all four Nickel-base alloys in air at 704°C. The gross section stress reanges from 145 MPa to 164 MPa.

Figure 16. Typical fractograph of a CCGR test in argon at 704°C. Surface shown in for Astroloy at 200X and the prior particle boundaries are clearly visible.

Figure 17. Typical fractograph of a CCGR test performed in air at 704°C. The surface shown is for Astroloy at 200X. The fracture surface does not follow the prior particle boundaries.

FIGURE 1

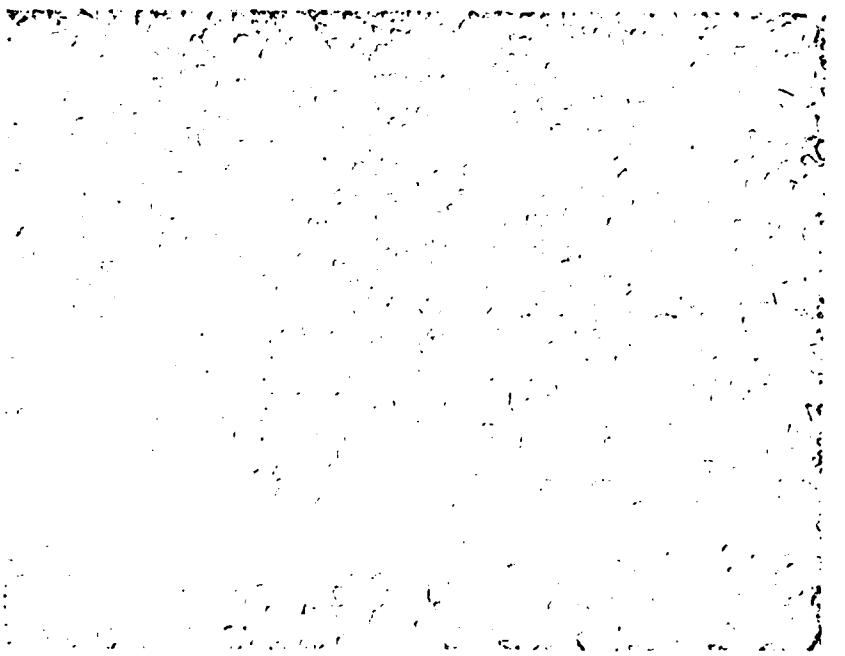

FIGURE 2

Copy available to DTIC does not permit fully legible reproduction

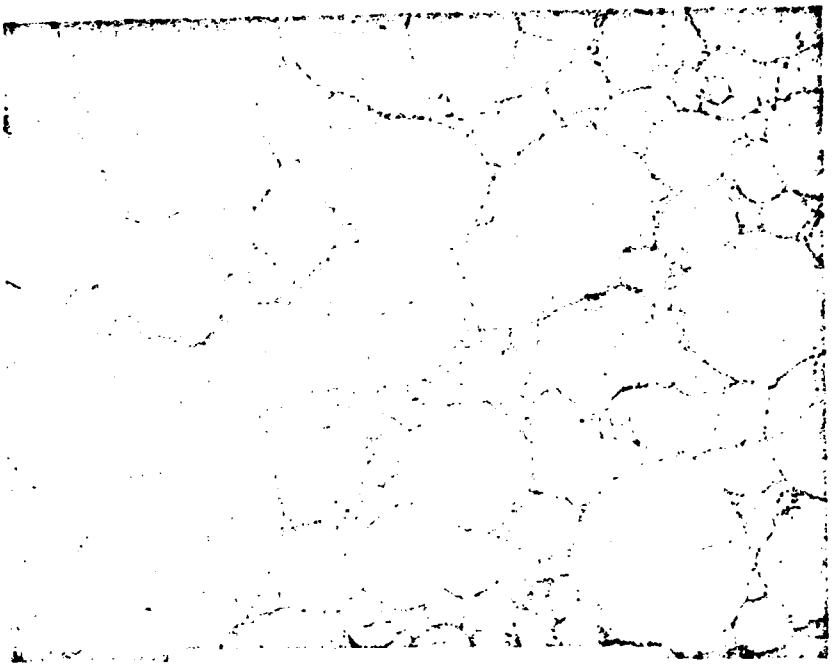

FIGURE 3

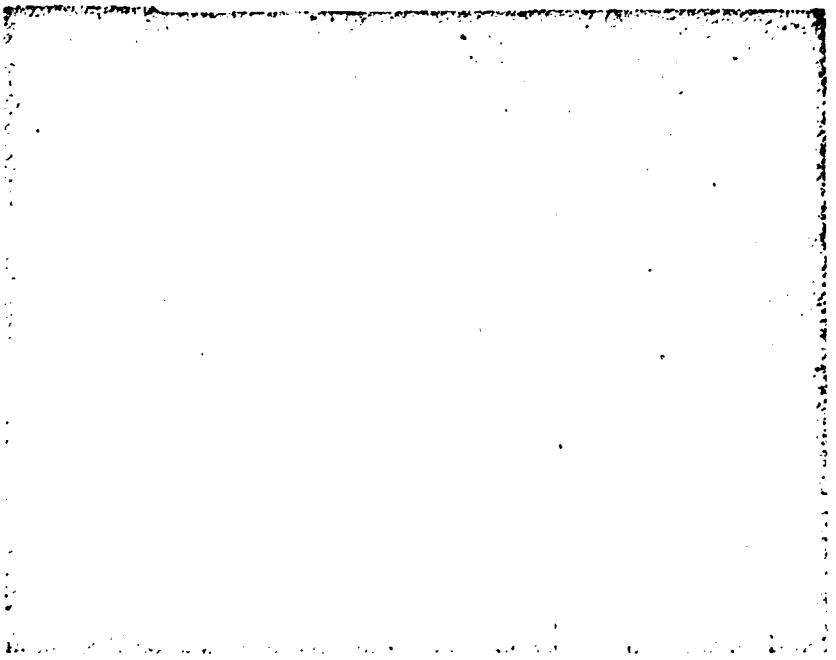

FIGURE 4

Copy ... DDC does not permit fully legible reproduction

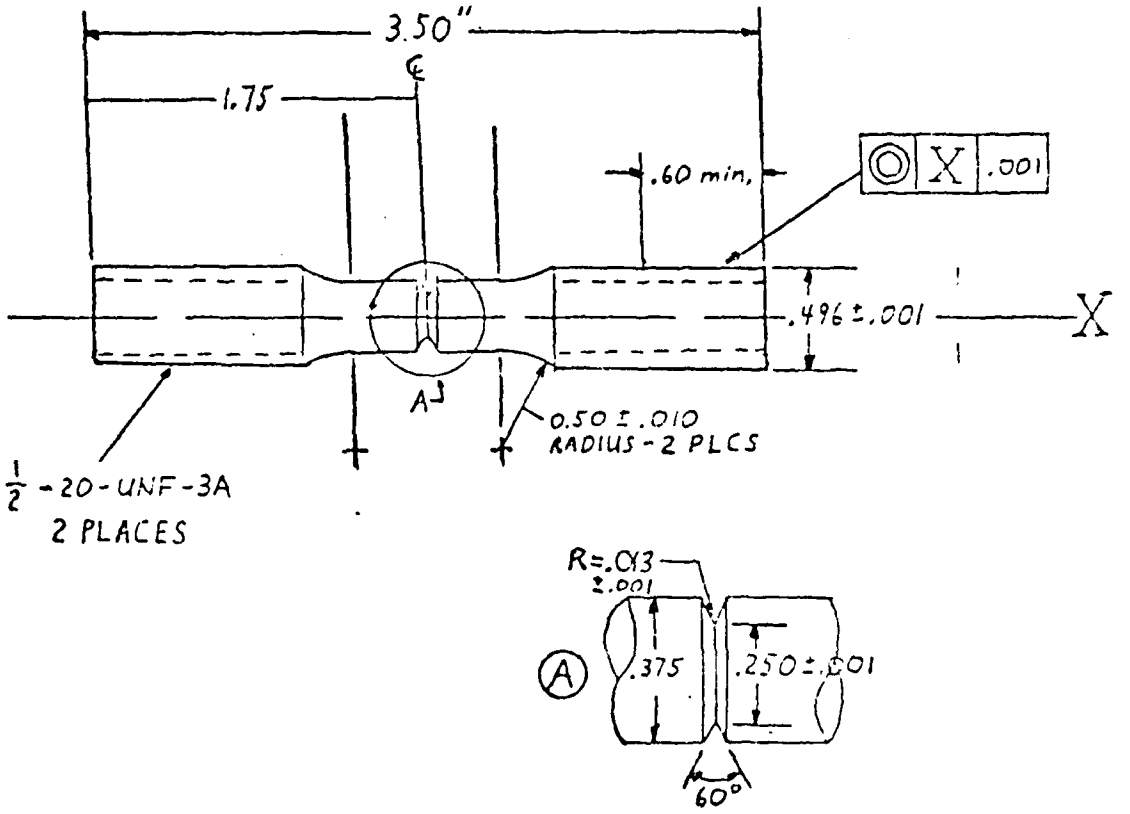
3.50"
1.75
.60 min.
.001
X
.496 ± .001
X
A
0.50 ± .010
RADIUS - 2 PLCS
½ - 20 - UNF - 3A
2 PLACES
R=.013
±.001
A
.375
.250 ± .001
60°

FIGURE 5

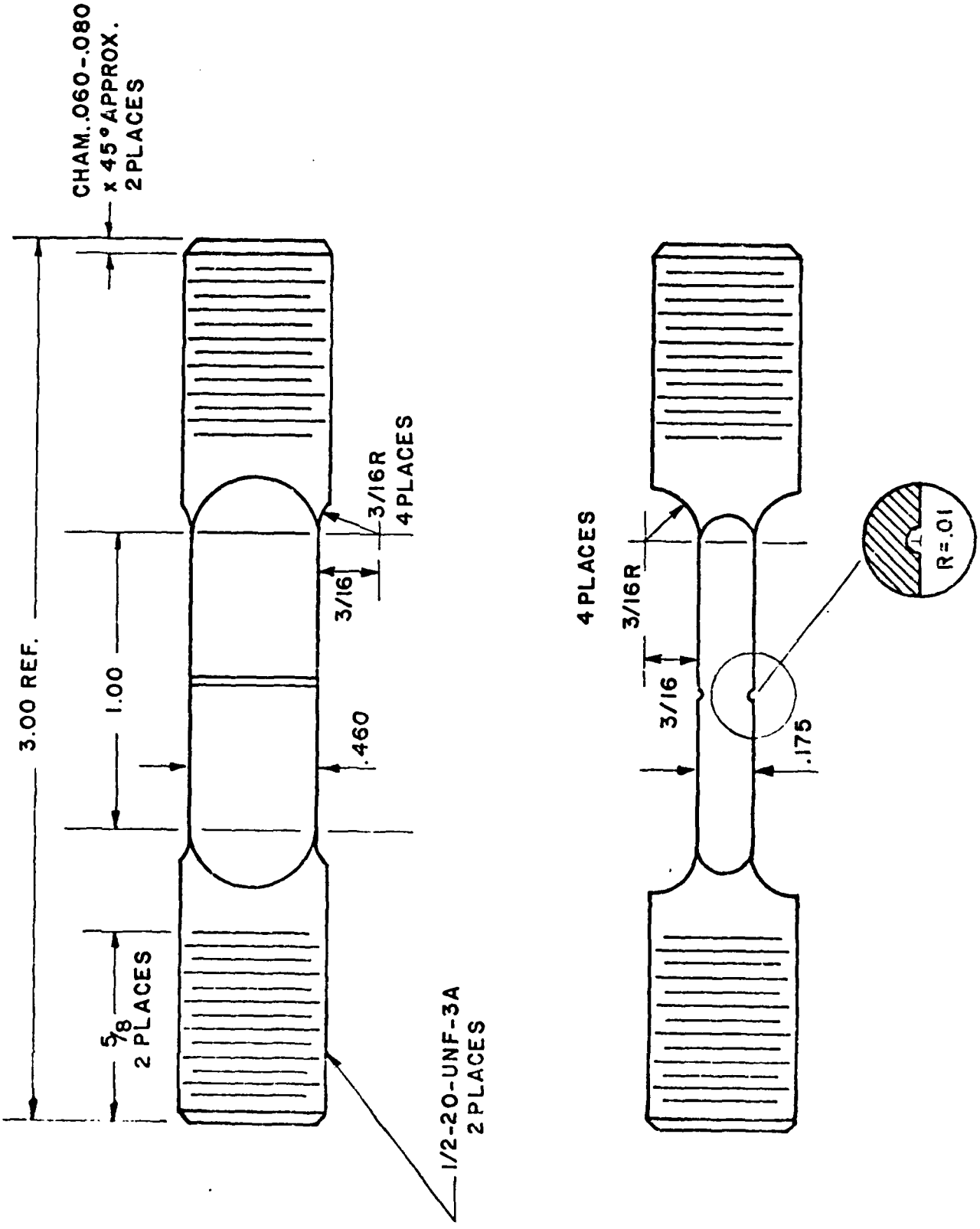
CHAM..060-.080
x 45° APPROX.
2 PLACES
3.00 REF.
1.00
3/16R
4 PLACES
3/16
.460
5/8
2 PLACES
1/2-20-UNF-3A
2 PLACES
4 PLACES
3/16R
3/16
.175
R=.01

FIGURE 6

FIGURE 7

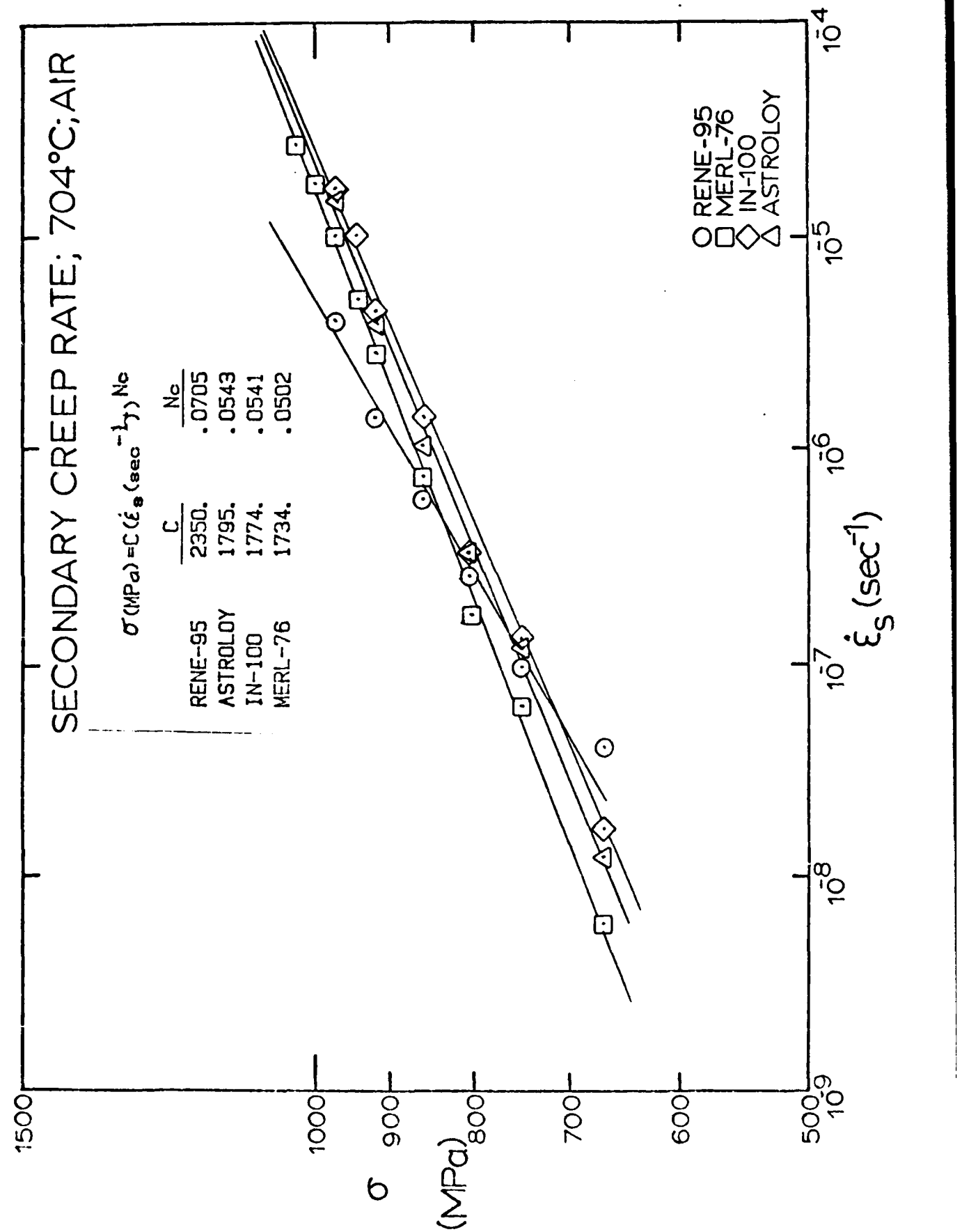
SECONDARY CREEP RATE; 704°C; AIR
σ(MPa) = C($\dot{\varepsilon}_s$(sec^{-1}))^{N_c}
C
RENE-95 2350.
ASTROLOY 1795.
IN-100 1774.
MERL-76 1734.
N_c
.0705
.0543
.0541
.0502
RENE-95
MERL-76
IN-100
ASTROLOY
σ (MPa)
$\dot{\varepsilon}_s$ (sec^{-1})
1500
1000
900
800
700
600
500
10^{-9}
10^{-8}
10^{-7}
10^{-6}
10^{-5}
10^{-4}

FIGURE 8

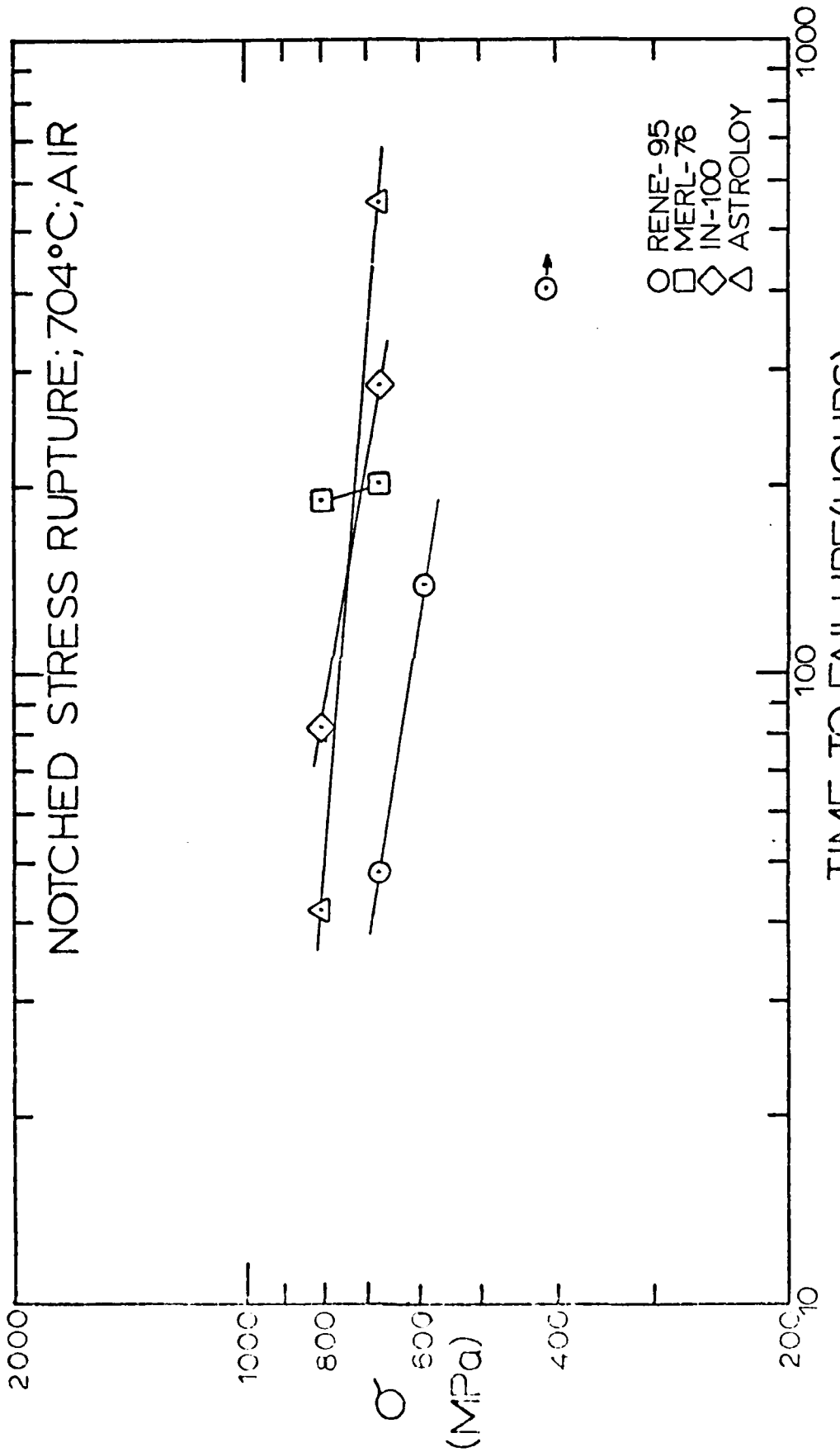
NOTCHED STRESS RUPTURE; 704°C; AIR
RENE-95
MERL-76
IN-100
ASTROLOY
TIME TO FAILURE(HOURS)
σ (MPa)
2000
1000
800
600
400
200
10
100
1000

FIGURE 9

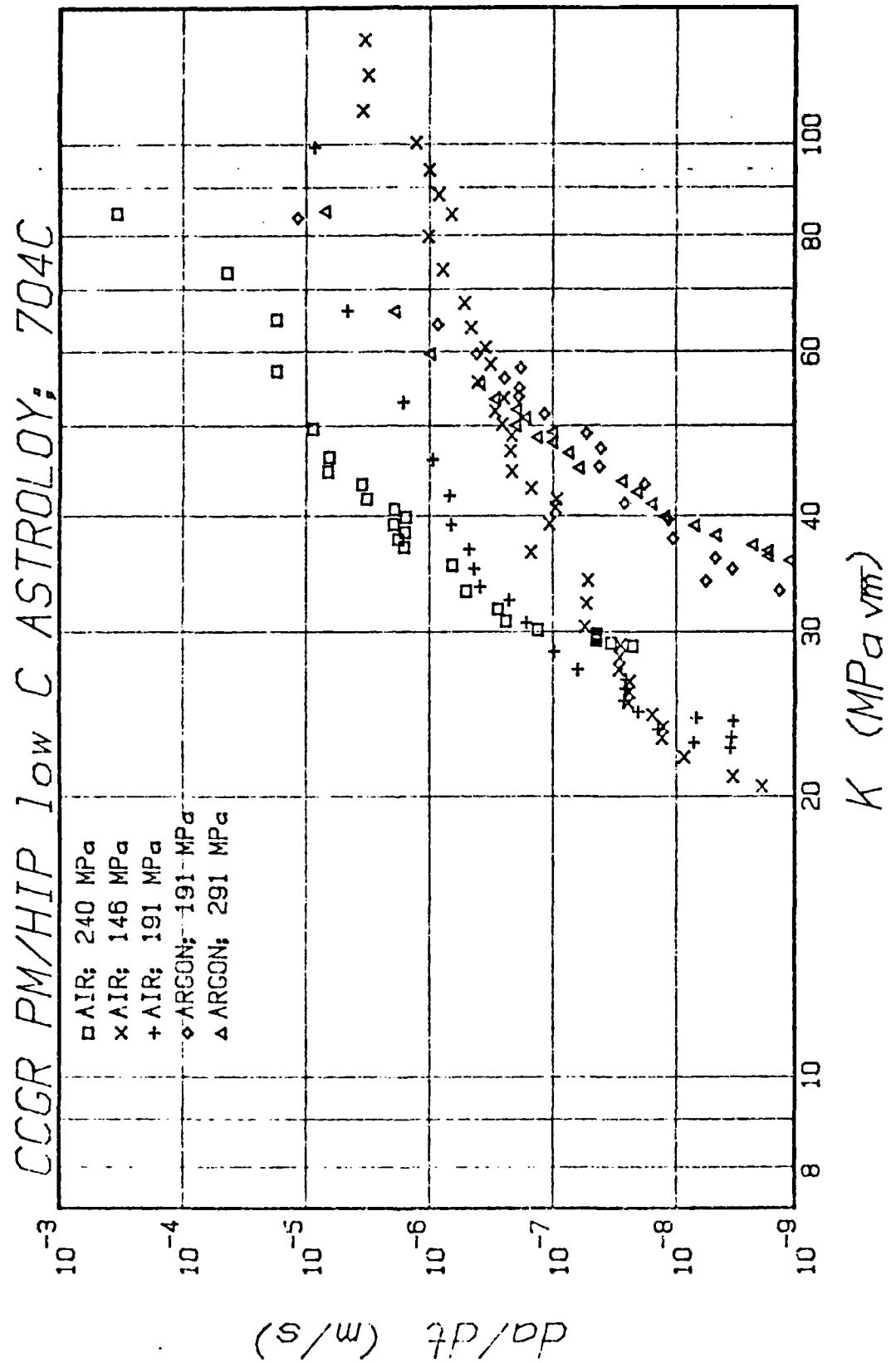
CCGR PM/HIP low C ASTROLOY; 704C
□ AIR; 240 MPa
× AIR; 146 MPa
+ AIR; 191 MPa
◇ ARGON; 191 MPa
△ ARGON; 291 MPa
da/dt (m/s)
K (MPa √m)
10^-3
10^-4
10^-5
10^-6
10^-7
10^-8
10^-9
8
10
20
30
40
60
80
100

FIGURE 10

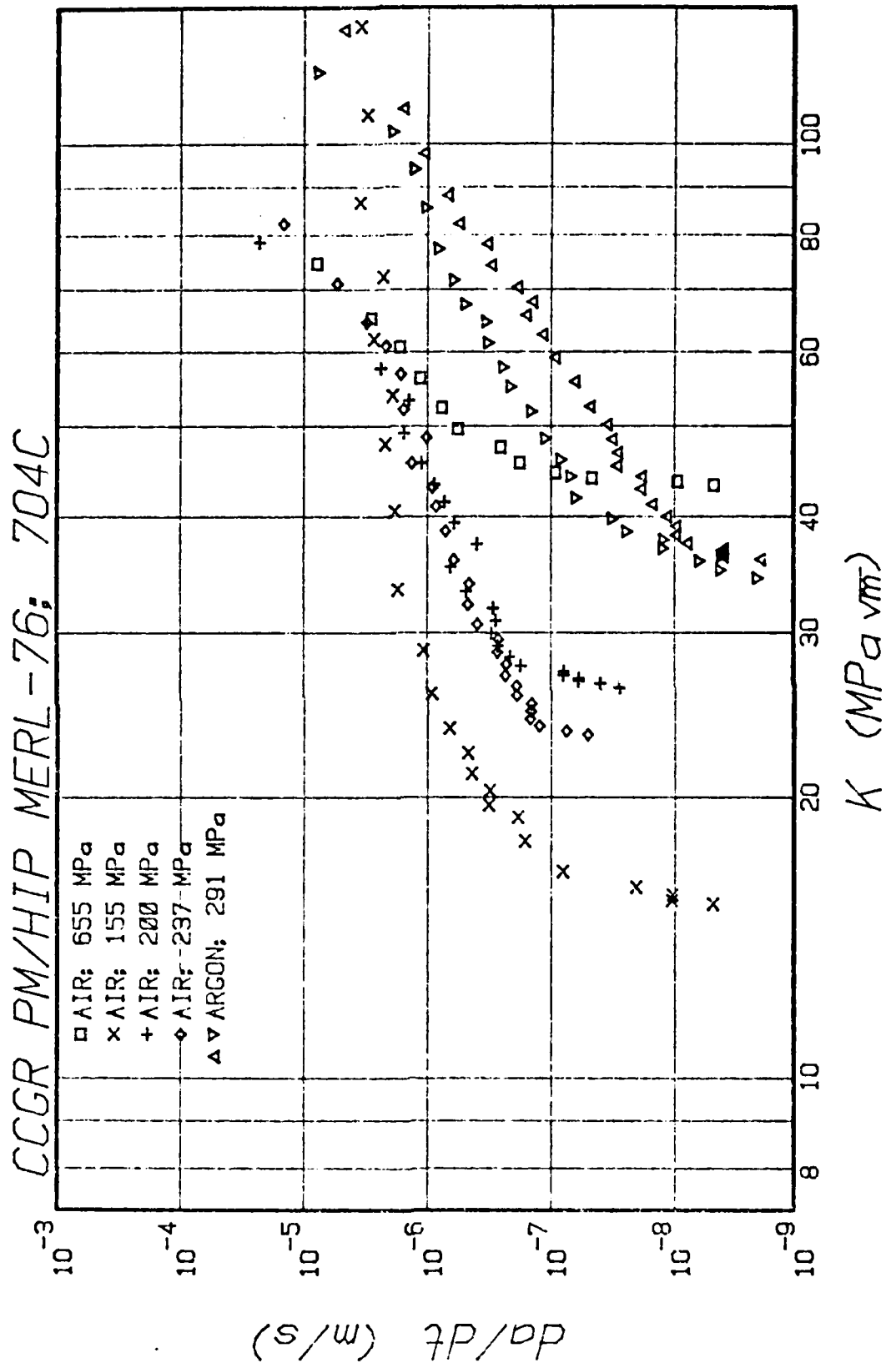
CCGR PM/HIP MERL-76; 704C
□ AIR; 655 MPa
× AIR; 155 MPa
+ AIR; 200 MPa
◇ AIR; 237 MPa
△▽ ARGON; 291 MPa
da/dt (m/s)
K (MPa √m)
10^-3
10^-4
10^-5
10^-6
10^-7
10^-8
10^-9
8
10
20
30
40
60
80
100

FIGURE 11

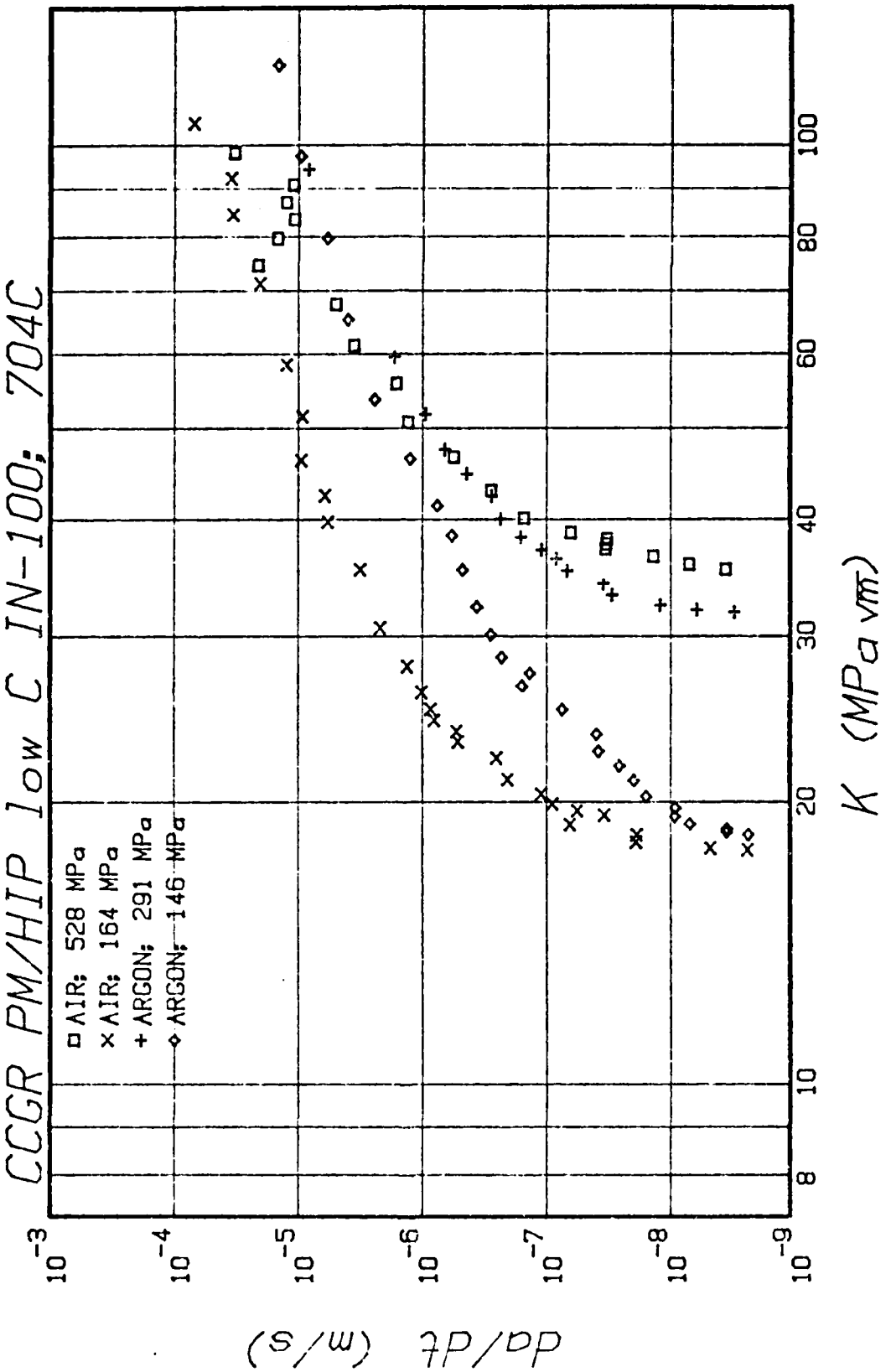
CCGR PM/HIP low C IN-100; 704C
AIR; 528 MPa
AIR; 164 MPa
ARGON; 291 MPa
ARGON; 146 MPa
da/dt (m/s)
K (MPa√m)
10^-3
10^-4
10^-5
10^-6
10^-7
10^-8
10^-9
8
10
20
30
40
60
80
100

FIGURE 12

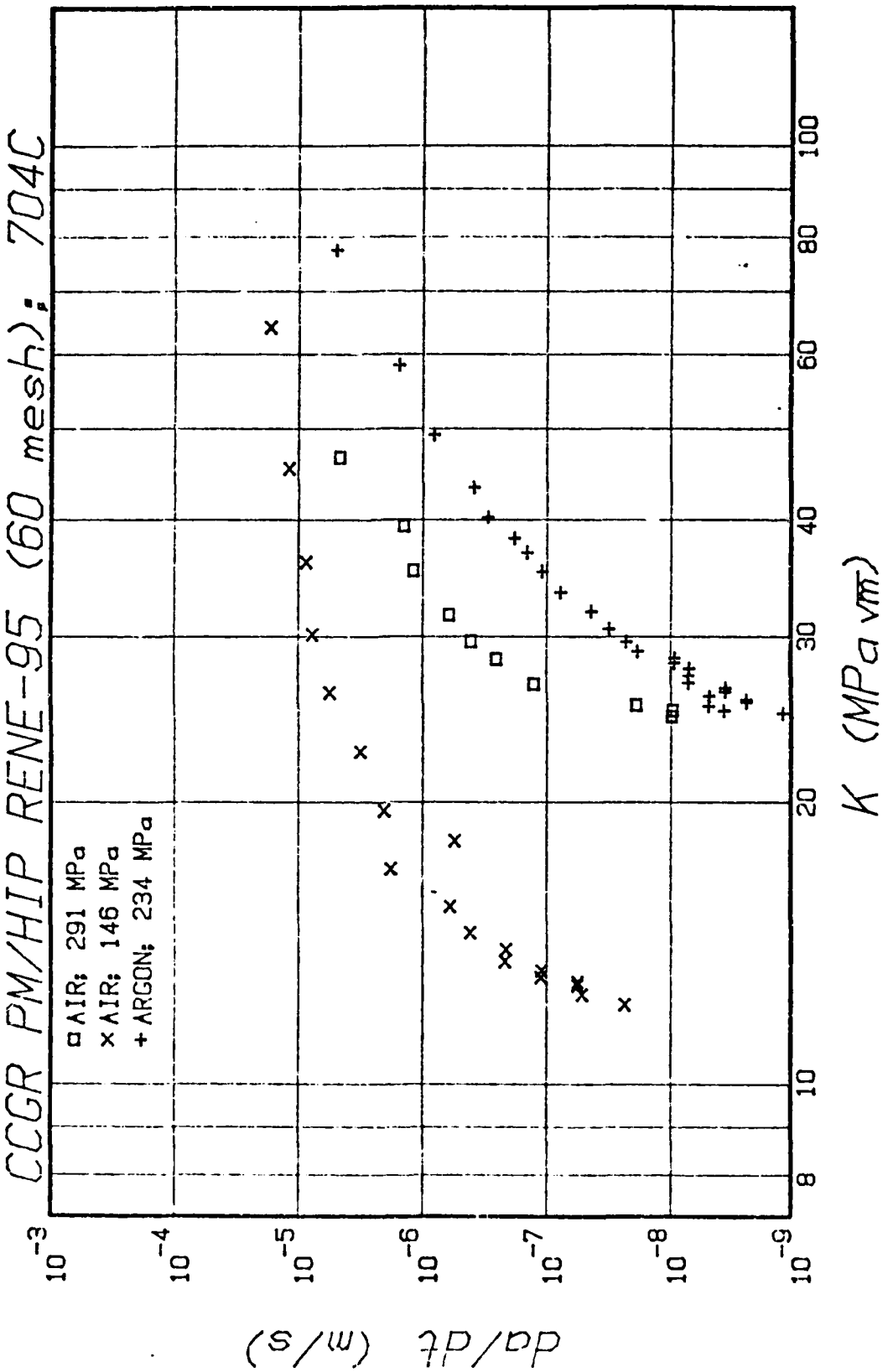
CCGR PM/HIP RENE-95 (60 mesh); 704C
□ AIR; 291 MPa
× AIR; 146 MPa
+ ARGON; 234 MPa
da/dt (m/s)
K (MPa √m)
10^-3
10^-4
10^-5
10^-6
10^-7
10^-8
10^-9
8
10
20
30
40
60
80
100

FIGURE 13

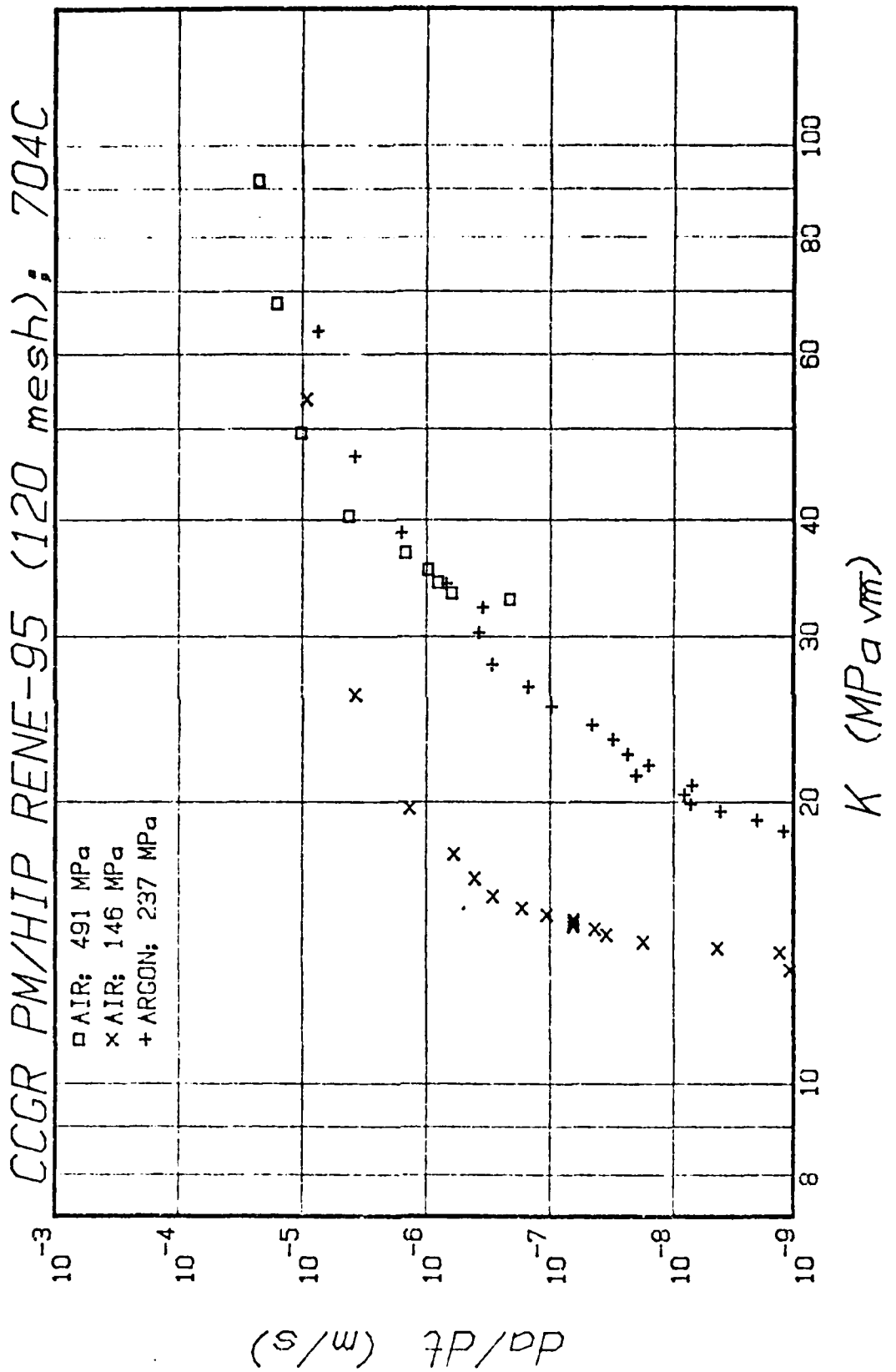
CCGR PM/HIP RENE-95 (120 mesh); 704C
□ AIR; 491 MPa
× AIR; 146 MPa
+ ARGON; 237 MPa
da/dt (m/s)
K (MPa √m)
10^-3
10^-4
10^-5
10^-6
10^-7
10^-8
10^-9
8
10
20
30
40
60
80
100

FIGURE 14

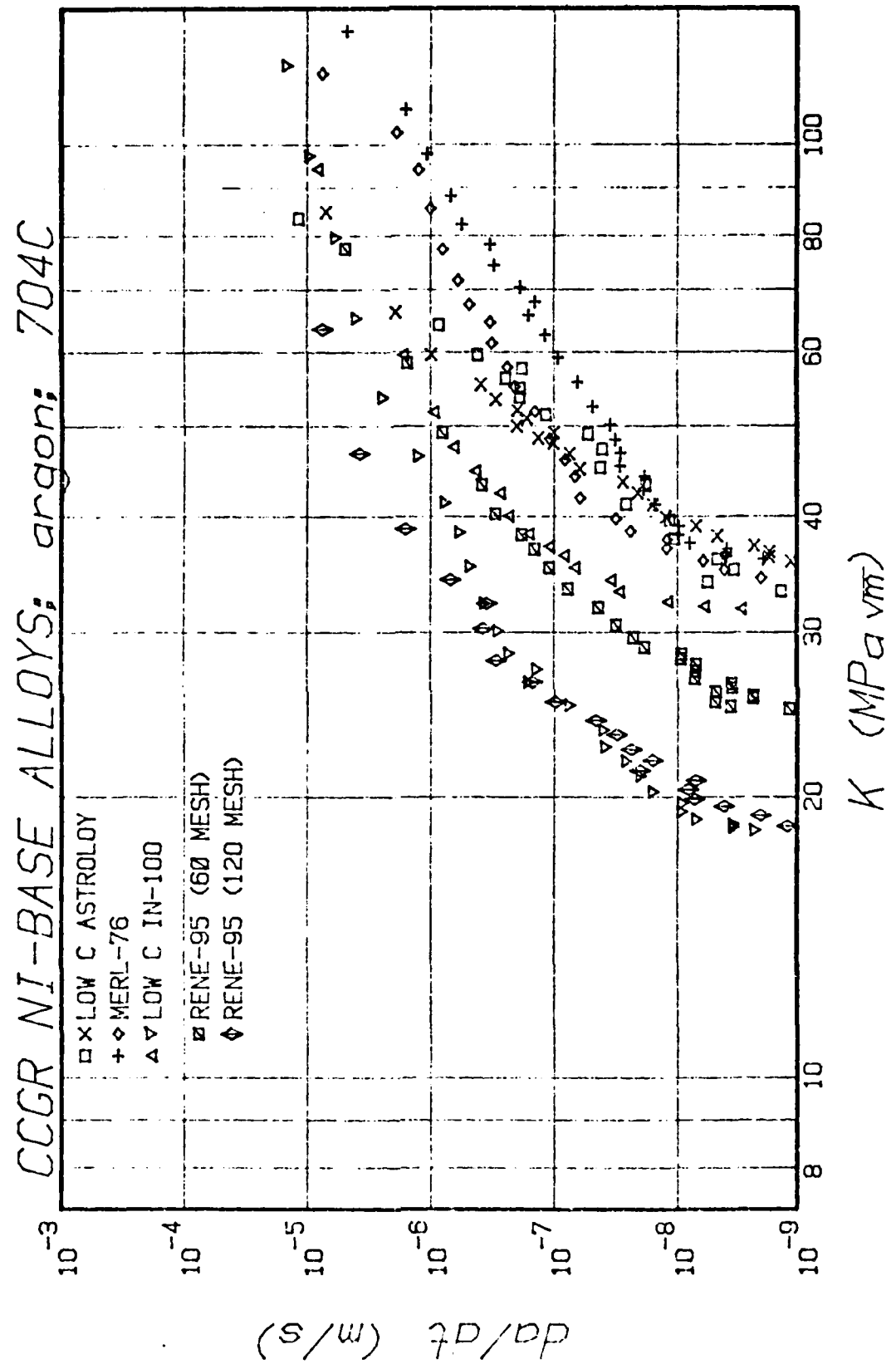
CCGR NI-BASE ALLOYS; argon; 704C
□×LOW C ASTROLOY
+◇MERL-76
△▽LOW C IN-100
⧄RENE-95 (60 MESH)
◆RENE-95 (120 MESH)
da/dt (m/s)
K (MPa √m)
10^-3
10^-4
10^-5
10^-6
10^-7
10^-8
10^-9
8
10
20
30
40
60
80
100

FIGURE 15

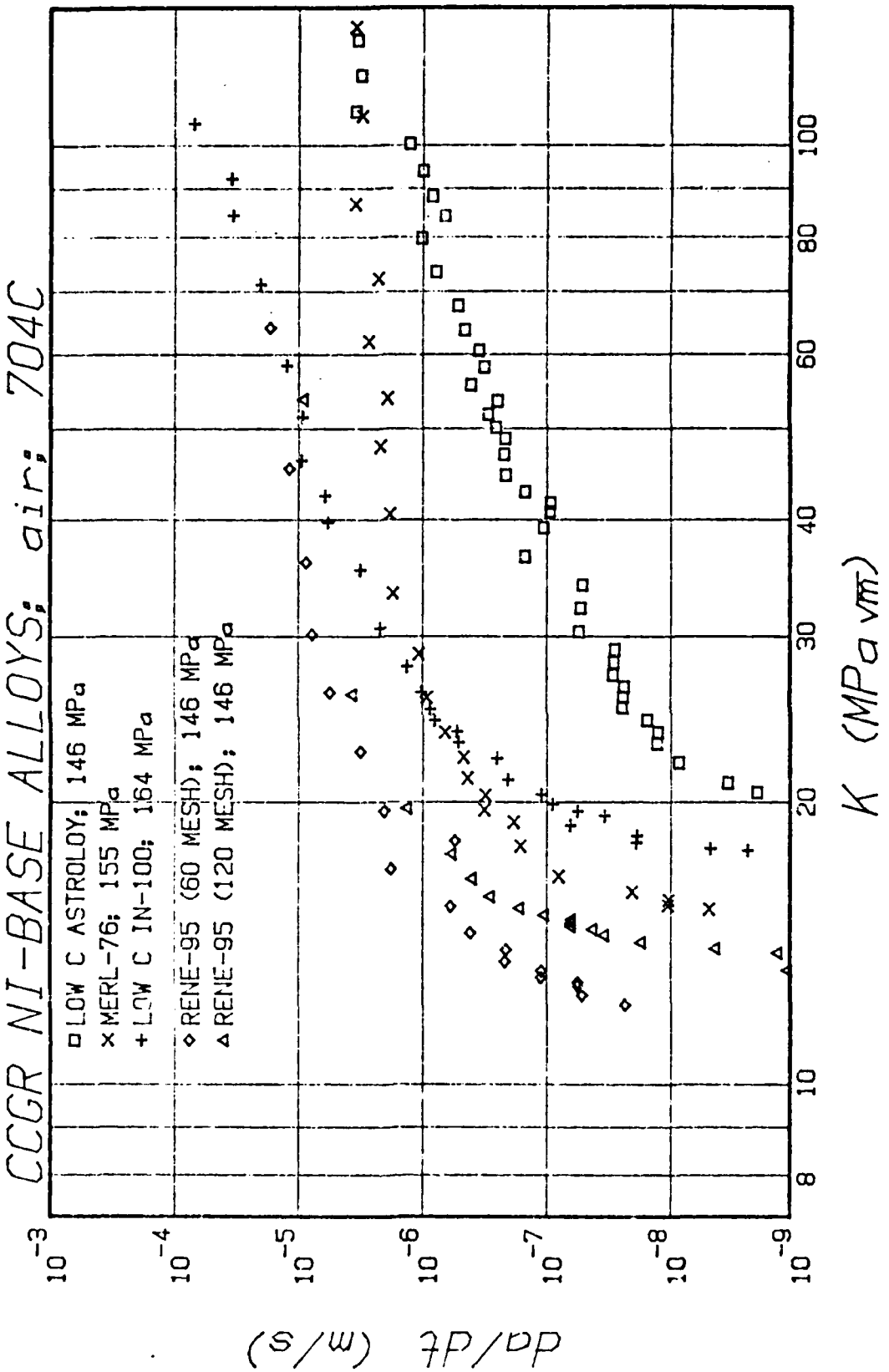
CCGR NI-BASE ALLOYS; air; 704C
□ LOW C ASTROLOY; 146 MPa
× MERL-76; 155 MPa
+ LOW C IN-100; 164 MPa
◇ RENE-95 (60 MESH); 146 MPa
△ RENE-95 (120 MESH); 146 MPa
da/dt (m/s)
K (MPa √m)
10^-3
10^-4
10^-5
10^-6
10^-7
10^-8
10^-9
8
10
20
30
40
60
80
100

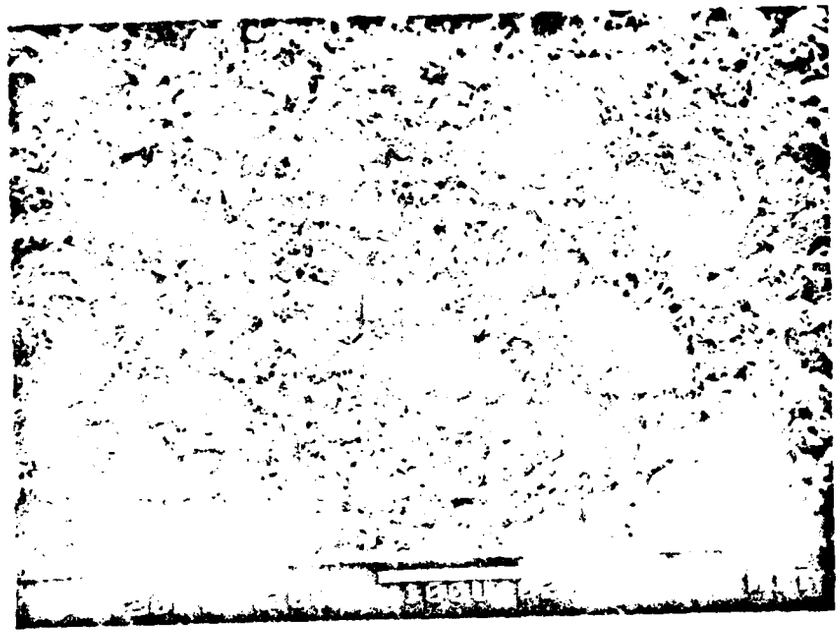

FIGURE 16

FIGURE 17

Copy available to DTIC does not permit fully legible reproduction

PART II

A STUDY OF CREEP CRACK GROWTH IN 2219-T851 ALUMINUM ALLOY USING A COMPUTERIZED TESTING SYSTEM

Philippe L. Bensussan
Graduate Student

ABSTRACT

Creep Crack Growth Rates were measured in high strength 2219-T851 Aluminum alloy with a computerized, fully automated test procedure. Crack growth tests were performed on CT specimens with side grooves. The experimental set-up is described. During a test, the specimen is cyclically loaded on a servohydraulic testing machine under computer control, maintained at maximum load for a given hold time at each cycle, unloaded and then reloaded. Crack lengths are obtained from compliance measurements recorded during each unloading. It is shown that the measured crack growth rates per cycle do represent Creep Crack Growth rates per unit time for hold times longer than 10 seconds.

The validity of LEFM concepts for side-grooved specimens is reviewed, and compliance and stress intensity factor calibrations for such specimens are reported. Creep brittle and creep ductile behaviors are discussed in terms of concepts of fracture mechanics of creeping solids. It is found that a correlation exists between Creep Crack Growth rates under plane strain conditions and the stress intensity factor ($da/dt = AK^{3.8}$ at 175°C) for simple K histories in a regime of steady or quasi-steady state crack growth.

Micromechanisms of fracture are determined to be of complex nature. The mode of fracture is found to be purely intergranular at low crack growth rates and mixed inter- and transgranular at high crack growth rates.

TABLE OF CONTENTS

	Introduction	3
I	Creep Brittle versus Creep Ductile Behaviors	3
II	Experimental Procedures	7
	1) Material Description	7
	2) Specimen Geometry	7
	3) Crack Length Measurement Technique	8
	4) Stress Intensity Factor Calculation	9
	5) Experimental Set-Up	10
III	Results and Discussion	11
	Conclusions	17
	References	18
	Figures	21
	Appendices	40

A STUDY OF CREEP CRACK GROWTH IN 2219-T851 ALUMINUM ALLOY USING A COMPUTERIZED TESTING SYSTEM

INTRODUCTION. Nickel base superalloy parts in jet engines, some stainless steel assemblies in nuclear and conventional power plants, titanium and aluminum alloy components used in hot sections of aircraft structures are all maintained in service at temperatures well within the creep regime (i.e. $T(°K)/T_m(°K) \gtrsim .4$).

It has been found that a single crack can often propagate at high temperatures under sustained load, mainly under the influence of creep and/or environment induced damages [1], [2], [3], [4], [5]. In order to estimate the remaining life of a component containing a measurable crack, crack growth tests have to be performed at these temperatures.

In the case where creep damage only is present, it is now well established that a crack propagates by nucleation, growth and coalescence of intergranular cavities on grain boundaries lying ahead of the crack tip [1], [6], [7], [8], [9], [10], [11], [12], [13]. Whether the role of an aggressive environment is to accelerate one of these stages or to cause damage of a completely different nature is still not clear in all cases [13]. Thus, we define Creep Crack Growth as "the propagation of a single macroscopic crack under sustained load at temperatures well within the creep regime", and no restriction about the exact nature of the damage is considered.

I) CREEP BRITTLE VERSUS CREEP DUCTILE BEHAVIORS

Materials susceptible to Creep Crack Growth (CCG) can be said to be either CREEP BRITTLE or CREEP DUCTILE. Creep brittle materials fail by CCG with almost no bulk creep deformation though creep ductile materials fail by CCG with extensive bulk creep deformation, even under small scale yielding conditions. For example, it has been shown that nickel base superalloys are creep brittle [1], [2], [5], [14] at temperatures as high as 760°C and 304 stainless steel is creep ductile [15] at temperatures as low as 538°C. The distinction between these two extreme behaviors can be rationalized to a certain extent by using concepts of FRACTURE MECHANICS of CREEPING SOLIDS which are reviewed below.

In a creeping stressed body, total strains are the sum of elastic (ε^{el}), plastic (ε^{pl}) and creep (ε^{cr}) strains. Around the tip of a crack in such a solid, elastic and plastic strains develop instantaneously as the load is applied, and, as time increases, creep strains build up, in particular close to the crack tip where stresses, and thus creep strain rates, are very high. In the case of a stationary sharp crack loaded in Mode I, the stress field ahead of the crack tip can be mapped in the following manner:

In the elastic region where the elastic strains are dominant, the stresses for small scale yielding conditions, are well approximated by the usual singular field [16]:

$$\sigma_{ij} = \frac{K_I}{\sqrt{2\pi r}} f_{ij}(\theta) \qquad \text{(I-1)}$$

where K_I is the stress intensity factor.

In the plastic region where the plastic strains are dominant, if the plastic behavior of the material can be modeled by a power law:

$$\varepsilon^{pl} = B_p \sigma^{n_p} \qquad \text{(I-2)}$$

the stresses are well-represented by the HRR singularities [17], [18], [19], given by

$$\sigma_{ij} = \left[\frac{J}{B_p I_{n_p} r}\right]^{1/(n_p+1)} \tilde{\sigma}_{ij}(\theta, n_p) \qquad \text{(I-3)}$$

where the loading parameter is now the J-integral [20], and $I_{n_p} \geq \pi$.

As time increases, these stresses are relaxed by creep. If the material is assumed to creep according to a power law:

$$\dot{\varepsilon}^{cr} = B_c \sigma^{n_c} \qquad \text{(I-4)}$$

and if the plastic strains are neglected, in the region where the creep strain rates are dominant, the stresses are given by the time dependent RR singular field [21] analogous to the HRR field:

$$\sigma_{ij}(t) = \left[\frac{C(t)}{B_c I_{n_c} r}\right]^{1/(n_c+1)} \tilde{\sigma}_{ij}(\theta, n_c) \qquad \text{(I-5)}$$

The loading parameter C(t) can be calculated as:

$$t < t_{tr} \quad C(t) = \frac{J}{(n_c+1)t} \qquad \text{(1-6a)}$$

$$t > t_{tr} \quad C(t) = C^* \qquad \text{(I-6b)}$$

where C* is the time independent C* integral [22], and t_{tr} the transition time:

$$t_{tr} = \frac{J}{(n_c+1)C^*} \qquad \text{(I-6c)}$$

For long times ($t > t_{tr}$), the stresses at the crack tip are fully relaxed and the whole specimen tends toward a steady state of stress. Thus, this transition time really marks a transition between a regime of localized creep deformations at the crack tip and a regime of extensive creep conditions.

Though this whole analysis assumes that the crack remains stationary, it can still be used in a very conservative way to predict whether a material is creep brittle. If the transition time for a specimen in which a crack is stopped is much larger than the time to failure for an identical specimen in which the crack is allowed to grow, creep deformations will certainly remain localized at the crack tip even during a crack growth test. Thus, such a material is expected to be creep brittle. Yet, if the reverse is true, no conclusion can be unambiguously drawn.

Since for small scale yielding conditions:

$$J \sim K_I^2/E \qquad [20]$$

the stress, strain rate and strain distributions around the tip of a stationary sharp crack are completely determined at short times ($t < t_{tr}$) when K_I is known. Thus, the only natural loading parameter to correlate crack growth rates under small scale yielding conditions in creep brittle materials is the stress intensity factor.

This correlation has been successfully tried for nickel base superalloys [1], [2] and for 2219-T851 aluminum alloy [23]. Yet, correlations of da/dt versus C* have been used for creep ductile materials such as 304 stainless steels [15], chromium-molybdenum-vanadium steel [24], and for aluminum alloys such as RR58 [25] (for which K [26] and J [27] have also been proposed) and 6061 [28].

The spatial distribution ahead of the crack tip of the tensile stress across the crack plane has been calculated for 2219-T851 at 175°C as a function of time for conditions typical of the crack growth tests presented below. The calculations were carried out on the basis of data listed in Table I-1 and the results are shown in Figure 1. K was obtained according to [29] and C* by analogy to the method developed for J in [30]. From $K = 20.8\ MPa\sqrt{m}$ and $C^* = 4.3 \times 10^{-24}$ MPa.m.s.$^{-1}$, the transition time was determined:

$$t_{tr} = 7 \times 10^{19}\ s \qquad (I\text{-}7)$$

which is much larger than a typical time to failure:

$$t_f \sim 1.4 \times 10^{5}\ s \qquad (I\text{-}8)$$

Thus, 2219-T851 can be expected to be creep brittle at 175°C. The same conclusion can be drawn using the scaling time introduced by McClintock et al [31]:

$t_{tr} = \frac{\sigma^{\infty}}{E\dot{\varepsilon}_{\infty}}$ where σ^{∞} and $\dot{\varepsilon}_{\infty}$ are respectively the far field net section stress and the corresponding creep strain rate, which leads to

$$t_{tr} = 1 \times 10^{34}\ s \qquad (I\text{-}9)$$

TABLE I-1

MATERIAL:	2219-T851
TEMPERATURE:	175°C
SPECIMEN:	C.T., (T-L) orientation
	w = 6.35 cm, b_{net} = .76 cm, b = 1.27 cm
YOUNG'S MODULUS:	$E = 7.1 \times 10^{4}$ MPa
YIELD STRESS:	Y = 297 MPa
PLASTIC LAW:	$\varepsilon^{pl} = 7.7 \times 10^{-70} \sigma^{27}_{(MPa)}$
CREEP LAW:	$\dot{\varepsilon}^{Cr}_{(s^{-1})} = 1.2 \times 10^{-63} \sigma^{24}_{(MPa)}$
LOAD:	P = 5344N
CRACK LENGTH:	a = 3.18 cm (a/w = 0.5)

II) EXPERIMENTAL PROCEDURES

1) MATERIAL DESCRIPTION

The reported work was performed on 2219 commercial aluminum alloy. The alloy was provided by "ALCOA" in the form of 1/2" thick rolled plates in the T851 temper [32] The handbook typical composition of this aluminum-copper alloy [33] is given in Table II-1.

TABLE II-1
Chemical Composition of 2219 Aluminum Alloy (w%)

Cu	Mn	Zr	V	Ti	Si	Fe	Mg	Zn	Other	Al
6.3	.3	.18	.10	.06	<.2	<.3	<.02	<.10	<.05 .15 max total	Bal.

The average grain dimensions in the rolling, long and short transverse directions are respectively approximately:

50 μm x 50 μm x 25 μm

2) SPECIMEN GEOMETRY

ASTM CT specimens [29] were machined from the as received plates in the (T-L) and (L-T) orientations. The dimensions of the specimens are (Figure 2):

$w = 2.5" = 6.35$ cm

$b = .5" = 1.27$ cm

The starter notch length is:

$a_o = 0.8" = 2.03$ cm

.1" or .05" deep side grooves were machined on most of the specimens.

Two 0.050" thick steel knife edges attached on the front face of the specimens above and below the notch allowed measurements of opening displacements, at a normalized distance .675"/2.5" = .27 ahead of the loading line.

3) CRACK LENGTH MEASUREMENT TECHNIQUE

Though the potential drop methods have been successfully used for nickel base superalloys and steels [34], the compliance method has been preferred in this study because of the expected lack of sensitivity of the electrical methods when applied to highly conductive alloys such as the aluminum alloys.

For CT specimens with no side grooves, a calibration of crack length versus compliance measured at the location of the knife edges has been obtained using the results reported in [35] (See Appendix 1):

$$\frac{a}{w} = 1.025 - 6.07807\ U + 47.1092\ U^2 - 509.145\ U^3 + 2417.19\ U^4 - 4064.67\ U^5 \qquad \text{(II-1)}$$

where U is defined by:

$$U = 1/((bE'\frac{\Delta v}{\Delta P})^{1/2} + 1) \qquad \text{(II-2a)}$$

with $E' = E$ under plane stress conditions (II-2b)

$E' = \frac{E}{(1 - \nu^2)}$ under plane strain conditions, (II-2c)

and where $bE'\frac{\Delta v}{\Delta P}$ is the normalized compliance as measured at the location of the knife edges.

An experimental calibration of crack length as a function of compliance was performed for specimens with 40% side grooves. In order to compile load-displacement data for different a/w values, either machined notches or fatigue cracks were introduced in 40% side-grooved CT specimens. In the latter case, the crack was propagated by fatigue between consecutive measurements of the compliance of the specimen, at R ratios alternatively equal to 0.5 and 0.05. This resulted in distinct bands on the fracture surfaces from which crack lengths were easily deduced.

The following least-square fit was obtained:

$$a/w = .943769 - 4.29331\ U + 38.0499\ U^2 - 698.674\ U^3 + 4721.32\ U^4 - 10886.8\ U^5 \qquad \text{(II-3)}$$

where U is defined as:

$$U = 1/((bE\frac{\Delta v}{\Delta P})^{1/2} + 1)$$

Large discrepancies were found between the compliance calibrations for specimens with 40% side grooves and for smooth specimens under both plane stress and plane strain conditions.

Replacing the thickness b by an empirical effective thickness defined by:

$$b_{eff} = b - (b - b_{net})^2/b \qquad \text{(II-5)}$$

in (II-2a) has been reported to take up to 50% side grooves into account [36]. A relatively good agreement was found between our experimental calibration (equations (II-3) and (II-4)) and this empirical one (equations (II-1) and (II-2) modified by (II-5)), under plane strain conditions for a/w ratios up to about 0.6, and under plane stress conditions for larger a/w values (figure 3).

In our study, crack lengths were calculated from compliance measurements at the location of the knife edges by using:

(1) the experimental calibration (II-3) for specimens with 40% side grooves;

(2) the calibration (II-1) under plane stress conditions for smooth specimens;

(3) the calibration (II-1) under plane strain conditions for specimens with 20% side grooves.

The validity of these choices was checked by directly measuring the actual initial and final crack lengths on the fracture surfaces of broken specimens.

4) STRESS INTENSITY FACTOR CALCULATION

The stress intensity factor K as a function of crack length to width ratio a/w was calculated for standard smooth CT specimens according to the classical equation ([29]):

$$K = \frac{P}{b\sqrt{w}} \frac{(2 + a/w)}{(1 - a/w)^{3/2}} f(a/w) \qquad \text{(II-6)}$$

$$\text{with } f(a/w) = .886 + 4.64 \frac{a}{w} - 13.32 \left(\frac{a}{w}\right)^2 + 14.72 \left(\frac{a}{w}\right)^3 - 5.6 \left(\frac{a}{w}\right)^4$$

For CT specimens with side grooves, the following well-accepted formula was used [37], [38] (See Appendix 2):

$$K = \frac{P}{\sqrt{b b_{net} w}} \frac{(2 + a/w)}{(1 - a/w)^{3/2}} f(a/w) \qquad \text{(II-7)}$$

where f(a/w) has already been defined.

An experimental verification of this K-calculation for 40% side grooved specimens was performed. By assuming that the location of the axis of rotation of the arms of the specimen was not largely affected by the presence of side grooves, the loading line compliance for specimens with 40% side grooves was estimated, from which an experimental stress intensity factor was calculated (see Appendix 3):

$$K_{exp} = \frac{P}{\sqrt{b b_{net} W}} \frac{(2 + a/w)}{(1 - a/w)^{3/2}} \left(.374907 + 6.52948 \frac{a}{w} - 10.5935 \left(\frac{a}{w}\right)^2 + .703939 \left(\frac{a}{w}\right)^3 + 6.28039 \left(\frac{a}{w}\right)^4\right) \qquad \text{(II-8)}$$

The stress intensity factors given by (II-7) and (II-8) differ by less than 10% for a/w up to .65. Since the applicability of the concepts of the Linear Elastic Fracture Mechanics is questionable for longer crack lengths, and since it was not possible to check the eventual non-correlation between the location of the axis of rotation of the arms of the specimen and the side grooves, the expression (II-7) was used with confidence in this study.

5) EXPERIMENTAL SET-UP

Crack growth tests are performed on an Instron 1350 servohydraulic testing machine under the control of a DEC PDP 11/23. An Instron environmental chamber is clamped to the frame of the testing machine. Load on the specimen is applied through stainless steel pull rods extending into the chamber, to which steel grips for CT specimens are attached.

The temperature is checked within ±2°C with a Chromel-Alumel thermocouple touching the specimen. Prior to testing, the temperature is allowed to fully stabilize for about two hours.

Opening displacements are measured using an Instron clip gage dynamic extensometer attached, outside the furnace, to a long tubular steel extensometer spring-loaded against the knife edges on the specimen.

Prior to high temperature testing, the specimens are all fatigue-precracked at room temperature under computer control. They are then brought to high temperature and tested, also under computer control.

In this study, the results of two categories of crack growth tests are reported:

(1) CREEP CRACK GROWTH tests, where the applied load cycle includes a hold time at maximum load;

(2) FATIGUE CRACK GROWTH tests, where the applied load cycle does not include any hold time at maximum load.

For the first category of tests, a new software package for the real time control and the data reduction tasks has been developed(*). An already available Instron software package was used for the second category of tests.

III. RESULTS AND DISCUSSION

For hold times of 10, 30, 100, 300 and 1000 seconds, 10 seconds loading and unloading times, R = 0.5 and P_{max} = 5344N, crack growth rates per cycle ($\frac{da}{dN}$) increase with increasing hold times (Figure 4). This shows that, as expected, time dependent damage is encountered in addition to cyclic damage. In particular, even for the shortest hold times, $\frac{da}{dN}$ is larger than $1/2\Delta CTOD(\sim 4\frac{\Delta K^2}{YE}$[41]).

Crack Growth Rates per unit time ($\frac{da}{dt}$) were calculated for these tests as:

$$\frac{da}{dt} = \text{frequency} \times \frac{da}{dN}$$

and all the data fall in a narrow scatter band (Figure 5). Since no growth can take place during the short hold time (5 sec) elapsed at minimum load because of the residual stresses at the crack tip, only the hold time and the loading and unloading times are taken into account to estimate the cycle frequency. Assuming that crack growth during loadings and unloadings is independent of hold times, and is thus relatively less significant the longer the hold time, the data in the scatter band of Figure 8 represent time-dependent $\frac{da}{dt}$ -controlled crack growth.

Crack Growth Rates are found to be identical in the (T-L) and (L-T) orientations which can be accounted for by the microstructural equivalence of the transverse and rolling directions in our material.

(*) See: P. L. Bensussan, D. A. Jablonski, R. M. Pelloux: A Study of Creep Crack Growth in 2219-T851 Aluminum Alloy using a Computerized Testing System, Instron Corporate Research and Application Laboratory Report, January 1983. (To be published)

It is found that a decrease of the R ratio from 0.5 down to 0.05 does not affect the crack growth rates $\frac{da}{dt}$. Thus the maximum stress intensity factor K and not the stress intensity factor range ΔK drives crack growth.

For all the constant maximum load tests whose results are discussed above, the following test parameters were kept constant:

- CT specimens with 40% side grooves;
- Maximum load = 5344N (= 1200 lbs);
- Initial stress intensity factor $\simeq$ 16 MPa$\sqrt{m}$.

The crack growth curves $\frac{da}{dt}$ versus K for all these constant maximum load tests show three stages, schematically presented in Figure 6. Stage I corresponds to an initial transient regime where $\frac{da}{dt}$ varies very rapidly with K. In stage II, the data can be fitted to a power law of the form:

$$\frac{da}{dt} = A\ K^n \qquad \text{(III-1)}$$

The exponent "n" has often been reported in the literature as being comparable to the creep exponent "n_c" [42], [43] . This is not the case for our results where $n \simeq 3.8$ which is much smaller than n_c ($n_c = 24$). Finally, stage III corresponds to fast fracture which occurs when the maximum stress intensity factor reaches K_{IC}. Whether this three stage behavior and the correlation of equation (III-1) are material-dependent only or not, is discussed now.

For a given stress intensity factor, crack growth rates in specimens with 40% side grooves are very slightly higher than in specimens with 20% side grooves, but more than 10 times higher than in specimens with no side grooves (figure 7). In the latter case, severe crack bowing occurred, along with the development of very wide plane stress shear lips, and both these phenomona can explain the rather wavy nature of the crack growth curve. Yet, the 40% side grooves are sharp and deep enough to insure plane strain conditions through the net thickness of the specimens, as shown by the absence of shear lips, and the straight crack front markings on the fracture surfaces of the broken specimens. In addition, failure always occurred at stress intensity factors close to K_{IC} ($\simeq$ 35 MPa$\sqrt{m}$ [33]). Thus an upper limit of crack growth is reached under plane strain conditions.

The transient stage I regime of crack growth (in Figure 6) is only a function of the initial stress intensity factor, and is not a threshold for crack growth at all. This can be seen on Figure 8 where results of tests with different initial stress intensity factors (16, 20 and 25 MPa$\sqrt{m}$) are plotted. Yet, the correlation (III-1) in the stage II regime is independent of the initial stress intensity factor (Figure 8).

In constant maximum stress intensity factor tests, K was maintained within ±0.2% from the target K(Figure 9a), for crack length to width ratios from .35 to .65. The crack growth rates for this whole range of crack lengths (from .87" = 2.21 cm to 1.60" = 4.06 cm) fall right in the scatter band of the results of the constant maximum load tests in the stage II regime (Figure 9b). The slight variations in average crack growth rates with crack lengths, which are actually negligible in view of the scatter in the previous results, could very well be explained by imprecisions in the determination of both crack lengths and stress intensity factors. In addition, these results demonstrate clearly (1) the validity of the application of LEFM global concepts to side grooved specimens, and (2) the precision of the K-correlation given by equation (II-7).

Thus, a steady state constant crack growth rate corresponds to a constant K. In this regime, the crack blunting rate and the creep stress relaxation rate on the one hand, and the damage accumulation rate on the other hand, reach a balance. In addition, in the stage II regime of crack growth in constant load experiments, a quasi-steady state crack growth is established, where the balance described above is very slowly displaced as the stress intensity factor increases with crack length. It can thus be concluded that, for simple K histories such as the ones followed in constant maximum load or constant maximum stress intensity factor tests, the correlation between $\frac{da}{dt}$ and K given by equation (III-1) is valid in the quasi-steady or steady state crack growth. The existence of this correlation, which implies the applicability under certain conditions of the LEFM concepts to Creep Crack Growth, is comforting since 2219-T851 behaves in a typical creep brittle fashion at 175°C in air.

The two parameters of the $\frac{da}{dt}$ - K correlation ("A" and "n") are not functions of the hold time, the initial stress intensity factor and the R ratio. Both "A" and "n" change with temperature, n varying quite slowly (from n = 3.4 at 150°C, to n = 3.8 at 175°C and n = 4.8 at 198°C). As expected, crack growth rates increase with temperature (Figure 10).

Fruitless attempts to study more complex K histories, such as the ones encountered in decreasing K experiments, were performed: problems arose at low growth rates where oxide growth in the crack led to erroneous measurements of compliance (in one example, the difference between the measured crack length of an apparently stopped crack and the actual crack length was found, by reloading the specimen to a higher load, to be as high as 30 mils). However, for higher crack growth rates, one can expect the $\frac{da}{dt}$ - K correlation to remain valid if the stress intensity factor is decreased by "small enough" steps, and if it is maintained at constant levels for "long enough" times, to ensure that the conditions of quasi-steady crack growth can be maintained. Otherwise, the crack would dramatically slow down and eventually stop not only because of residual stresses at the crack tip but also because of the fact that the damage ahead of the crack is not critical anymore, and the crack tip might be largely blunted.

For Fatigue Crack Growth tests with a triangular wave shape with R = 0.05, crack growth rates per cycle ($\frac{da}{dN}$) at a given maximum stress intensity factor are independent of frequency in the range 0.02 Hz - 3 Hz (Figure 11). This is clearly emphasized by the solid symbols in Figure 12.

At a given maximum stress intensity factor, the following equation relating crack growth rates per cycle to crack growth rates per unit time for tests with hold times can be written (see open symbols in Figure 12):

$$\frac{da}{dN}\,(\text{frequency}) = \frac{1}{\text{frequency}} \cdot \frac{da}{dt}$$

where the frequency is calculated as explained previously, and $\frac{da}{dt}$ is not a function of hold time and frequency.

Thus, we measured in this study:

(1) CREEP CRACK GROWTH RATES, i.e., purely $\frac{da}{dt}$ controlled time-dependent crack growth, from results of tests with hold times of 10 seconds and longer;

(2) FATIGUE CRACK GROWTH RATES, i.e., purely $\frac{da}{dN}$ controlled cycle-dependent crack growth, from results of tests with no hold times and at frequencies of 0.02 Hz and higher.

For a frequency of 0.02 Hz, the much lower $\frac{da}{dN}$ for a triangular wave shape than for a trapezoidal one, at the same maximum K, clearly demonstrates the highly damaging effect of a hold time at maximum load.

Due to the complexity of the microstructure of 2219 Aluminum alloy, it is very difficult to determine unambiguously the micromechanisms of crack growth from SEM fractographs.

For Creep Crack Growth tests, dominant intergranular damage can be seen at low crack growth rates ($K \lesssim 20$ MPa$\sqrt{m}$) (Figure 13). At higher crack growth rates ($K \gtrsim 25$ MPa$\sqrt{m}$), both intergranular and transgranular cavitations develop, with the cavities nucleating at intermetallic particles (Figure 14). This somewhat mixed mode gives rather similar but much rougher fracture surfaces than the ones encountered in critical fast fracture ($K \gtrsim 35$ MPa$\sqrt{m}$), where damage is purely of the ductile transgranular type.

Fracture surfaces for Fatigue Crack Growth tests at low frequencies ($\lesssim 0.1$ Hz) look like the ones observed for Creep Crack Growth tests, and show mixed intergranular and transgranular damages (figure 15). Yet, evidences of more extensive rubbing are apparent due to the low R ratio (R = 0.05), and some brittle and ductile fatigue striations can be seen at some places. At higher frequencies ($\gtrsim 1$ Hz), ductile and brittle transgranular fatigue striations are dominant (figure 16).

The dominance of transgranular modes of fracture can be explained by the large amount of second phase particles in the bulk of the grains.

To close this section, the descriptions of the tests discussed above are summarized in Table III-1.

TABLE III-1

SPEC ID	ORIENT	SIDE GROOVES (%)	TEMP (°C)	ENVIR	TYPE OF TEST	R	FREQUENCY (H_z)	HOLD TIME(s)	LOADING TIME(s)	INITIAL K_{max}(MPa$\sqrt{m}$)
19A04	(L-T)	40	175	AIR	CGR,P=5344N	0.5	-	var.	10	~16
19B01	(T-L)	40	175	AIR	CGR,P=5344N	0.5	-	var.	10	~18
19B03	(T-L)	40	175	AIR	CGR,P=5344N	0.5	9.8×10^{-4}	1000	10	~16
19B04	(T-L)	40	175	AIR	CGR,P=5344N	0.5	3.1×10^{-3}	300	10	~16
19B02	(T-L)	40	175	AIR	CGR,P=5344N	0.5	8.3×10^{-3}	100	10	~16
19B05	(T-L)	40	175	AIR	CGR,P=5344N	0.5	0.02	30	10	~16
19B07	(T-L)	40	175	AIR	CGR,P=5344N	0.5	0.03	10	10	~16
19B06	(T-L)	40	175	AIR	CGR,P=5344N	0.05	8.3×10^{-3}	100	10	~16
19B18	(T-L)	0	175	AIR	CGR,P=6681N	0.5	9.8×10^{-4}	1000	10	~16
19B17	(T-L)	20	175	AIR	CGR,P=6140N	0.5	3.1×10^{-3}	300	10	~16
19B10	(T-L)	40	175	AIR	CGR,P=6681N	0.5	8.3×10^{-3}	100	10	~20
19B19	(T-L)	40	175	AIR	CGR,P=8017N	0.5	8.3×10^{-3}	100	10	~25
19B12	(T-L)	40	175	AIR	CGR,P=5344N	0.5	9.9×10^{-3}	100	1	~20
19B13	(T-L)	40	175	AIR	CGR,K=16MPa$\sqrt{m}$	0.5	3.1×10^{-3}	300	10	~16
19B11	(T-L)	40	175	AIR	CGR,K=20MPa$\sqrt{m}$	0.5	8.3×10^{-3}	100	10	~20
19B14	(T-L)	40	175	AIR	CGR,K=25MPa$\sqrt{m}$	0.5	8.3×10^{-3}	100	10	~25
19B15	(T-L)	40	198	AIR	CGR,P=5341N	0.5	8.3×10^{-3}	100	10	~16
19B16	(T-L)	40	175	AIR	FCP,P=5344N	0.05	0.02	-	-	~16
19B24	(T-L)	40	175	AIR	FCP,P=5344N	0.05	0.1	-	-	~16
19B08	(T-L)	40	175	AIR	FCP,P=5344N	0.05	1	-	-	~16
19B25	(T-L)	40	175	AIR	FCP,P=5344N	0.05	3	-	-	~16

CONCLUSIONS

1) A fully automated computerized experimental procedure was developed to study high temperature crack growth, and was applied to 2219-T851 Aluminum alloy. Crack growth tests were run on side-grooved CT specimens, and crack lengths were measured by the compliance technique. The validity of the application of LEFM concepts to side grooved specimens was reviewed, and satisfactory compliance and stress intensity factor calibrations were obtained. The compliance technique performed very well except at low crack growth rates, where oxide growth at the crack tip led to erroneous compliance measurements. The computerized testing system was reliable enough to conduct tests lasting several days.

2) Time-dependent Creep Crack Growth and cycle-dependent Fatigue Crack Growth were measured for 2219-T851 Aluminum Alloy at 175°C in air. In the case of Creep Crack Growth, the duration of the hold times at maximum load (>10 s) and loadings and unloadings are found to have no effect on crack growth rates per unit time. The absolute necessity of side grooving the specimens is demonstrated. 2219-T851 behaves as a typical creep brittle material, and a correlation exists between Creep Crack Growth rates under plane strain conditions and the maximum stress intensity factor — and not ΔK — ($\frac{da}{dt} = A(T)K^{n(T)}$), for simple K histories in the regime of steady or quasi-steady state crack growth. Yet, n(T) is not equal to the creep stress exponent.

3) The micromechanisms of crack growth have been investigated, and SEM fractographs show evidences of an essentially mixed intergranular and transgranular mode of fracture.

REFERENCES

[1] K. Sadananda, P. Shahinian: Creep Crack Growth Behavior and Theoretical Modelling, Met. Sci. J., 15, 1981, p. 425 - 432.

[2] L. S. Fu: Creep Crack Growth in Technical Alloys at Elevated Temperature--A Review, Eng. Fract. Mech., 13, 1980, p. 307 - 330.

[3] M. H. El Haddad, T. H. Topper, B. Mukherjee: Review of New Developments in Crack Propagation Studies, JTEVA, 9, 1981, p. 65 - 81.

[4] K. Sadananda, P. Shahinian, Crack Growth Under Creep and Fatigue Conditions, in Creep-Fatigue - Environment Interactions, Eds. R. M. Pelloux and N. S. Stoloff, AIME, 1980, p. 86 - 111.

[5] R. M. Pelloux, J. S. Huang: Creep-Fatigue-Environment Interactions in Astroloy, Ibid, p. 151 - 164.

[6] J. L. Bassani: Macro and Micro-Mechanical Aspects of Creep Fracture, in Advances in Aerospace Structures and Materials - I, Eds. S. S. Wang and W. J. Renton, ASME, 1981.

[7] J. L. Bassani: Creep Crack Extension by Grain-Boundary Cavitation, in Creep and Fracture of Engineering Materials and Structures, Eds. B. Wilshire and D. R. Owen, 1981, p. 329 - 344.

[8] J. L. Bassani, V. Vitek: Propagation of Cracks Under Creep Conditions, to Appear in the Proceedings of the 9th U.S. National Congress of Applied Mechanics, Eds. L. B. Freud and C. F. Shih.

[9] W. D. Nix, D. K. Matlock, R. J. Dimelfi: A Model for Creep Fracture Based on the Plastic Growth of Cavities at the Tips of Grain Boundary Wedge Cracks, Acta Met, 25, 1977, p. 495 - 503.

[10] R. J. Dimelfi, W. D. Nix: The Stress Dependence of the Crack Growth Rate During Creep, Int. J. of Fract., 13, 1977, p. 341 - 348.

[11] R. Raj, S. Baik: Creep Crack Propagation by Cavitation Near Crack Tips, Met. Sci. J., 14, 1980, p. 383.

[12] V. Vitek, T. Takasugi: Mechanisms of Creep Crack Growth, in Micro and Macro Mechanisms of Crack Growth, Eds. K. Sadananda, B. B. Rath and D. J. Michel, AIME, 1982, p. 107 - 118.

[13] K. Sadananda, P. Shahinian: High Temperature Time-Dependent Crack Growth, Ibid, p. 119 - 130.

[14] J. S. Huang: Fatigue Crack Growth and Creep Crack Growth of P/M HIP Low Carbon Astroloy at High Temperatures, Sc. D. Thesis, MIT, February, 1981.

[15] A. Saxena: Evaluation of C* for the Characterization of Creep-Crack-Growth Behavior in 304 Stainless Steel, ASTM STP 700, 1980, p. 131 - 151.

[16] D. Broek, Elementary Engineering Fracture Mechanics, Sijthoff and Noordoff ed.,1978.

[17] J. R. Rice, G. F. Rosengren: Plane Strain Deformation Near a Crack Tip in a Power Law Hardening Material, J. Mech. Phys. Solids, 16, 1968, p. 1 - 12.

[18] J. W. Hutchinson: Singular Behaviour at the End of a Tensile Crack in a Hardening Material, J. Mech. Phys. Solids, 16, 1968, p. 13 - 31.

[19] J. W. Hutchinson: Plastic Stress and Strain Fields at a Crack Tip, J. Mech. Phys. Solids, 16, 1968, p. 337 - 347.

[20] J. R. Rice: A Path Independent Integral and the Approximate Analysis of Strain Concentration by Notches and Cracks, J. of App. Mech., Trans. of ASME, 1968, p. 379 - 386.

[21] H. Riedel, J. R. Rice: Tensile Cracks in Creeping Solids, ASTM STP 700, 1980, p. 112 - 130.

[22] J. D. Landes, J. A. Begley: A Fracture Mechanics Approach to Creep Crack Growth, ASTM STP 590, 1976, p. 128 - 148.

[23] J. G. Kaufman, K. O. Bogardus, D. A. Mauney, R. C. Malcom: Creep Cracking in 2219-T851 Plate at Elevated Temperatures, ASTM STP 590, 1976. p. 149 - 168.

[24] K. M. Nikbin, G. A. Webster, C. E. Turner: Relevance of Nonlinear Fracture Mechanics to Creep Cracking, ASTM STP 601, 1976, p. 47 - 62.

[25] K. M. Nikbin, G. A. Webster: Temperature Dependence of Creep Crack Growth in Aluminum Alloy RR58, in Micro and Macro Mechanisms of Crack Growth, Eds. K. Sadananda, B. B. Rath and D. J. Michel, AIME, 1982, p. 137 - 148.

[26] J. L. Kenyon, G. A. Webster, J. C. Radon, C. E. Turner: An Investigation of the Application of Fracture Mechanics to Creep Cracking, in Proceedings of the International Conference on Creep and Fatigue at Elevated Temperature Applications, I. Mech. E., Conference Publication, 13, 1973, Paper #C156/73.

[27] C. M. Branco, J. C. Radon: Analysis of Creep Cracking by the J Integral Concept, in Proceedings of the International Conference on Engineering Aspects of Creep, I. Mech. E., 2, 1980, Paper #C210/80.

[28] V. M. Radhakrishnan, A. J. McEvily: A Critical Analysis of Crack Growth in Creep, J. of Eng. Mat. and Tech., Trans. of ASME, 102, 1980, p. 200 - 206.

[29] ASTM Standard E399-81, Standard Test Method for Plane-Strain Fracture Toughness of Metallic Materials, 1982 Annual Book of ASTM Standards. Part 10, ASTM, 1982, p. 611.

[30] V. Kumar, C. F. Shih: Fully Plastic Crack Solutions, Estimation Scheme, and Stability Analysis for the Compact Specimen, ASTM STP 700, 1980, p. 406 - 438.

[31] F. A. McClintock, J. L. Bassani: Problems in Environmentally-Affected Creep Crack Growth, in Three Dimensional Constitutive Relationships and Ductile Fracture, Eds. J. Zarka and S. Nemat-Nasser, Dourdan (1980), 1981, p. 119 - 141.

[32] Materials and Processing DATABOOK '81, Metal Progress, Mid-June 1981, p. 70.

[33] ASM Metals Handbook, 9th ed., Vol. 2.

[34] M. D. Halliday, C. J. Beevers: The d. c. Electrical Potential Method for Crack Length Measurements, in The Measurement of Crack Length and Shape During Fracture and Fatigue, ed. C. J. Beevers, EMAS, 1980, p. 85 - 112.

[35] A. Saxena, S. J. Hudak: Review and Extension of Compliance Information for Common Crack Growth Specimens, Int. Journ. of Fracture, 14, 1978, p. 453 - 468.

[36] C. F. Shih, H. G. deLorenzi: Elastic Compliances and Stress Intensity Factors for Side Grooved Compact Specimens, Int. Journ. of Fracture, 13, 1977, p. 544 - 548.

[37] C. N. Freed, J. M. Krafft: Effect of Side Grooving on Measurements of Plane Strain Fracture Toughness, Journal of Materials, 1, 1966, p. 770 - 790.

[38] P. LeFort, D. F. Mowbray: Calibration of the Side-Grooved Modified Wedge-Opening-Load Specimen, JTEVA, 6, 1978, p. 114 - 119.

[39] User's Guide for Instron - FCP Application Software, Instron, 1982.

[40] ASTM Standard E647-81, Standard Test Method for Constant-Load Amplitude Fatigue Crack Growth Rates above 10^{-8} m/cycle, 1982 Annual Book of ASTM Standards, Part 10, ASTM, 1982, p. 784 - 788.

[41] J. W. Hutchinson: A Course in Nonlinear Fracture Mechanics, Department of Solid Mechanics, The Technical University of Denmark, 1979, p. 79.

[42] S. Purushothaman, J. K. Tien: A Theory for Creep Crack Growth, Scripta Met., 10, 1976, p. 663 - 666.

[43] J. T. Barnby: Crack Propagation During Steady State Creep, Eng. Fract. Mech., 7, 1975, p. 299 - 304.

[44] C. J. Smithells. Metals Reference Book, Volume 2, Interscience Publishers Inc., 1955, p. 552.

LIST OF FIGURES

Figure 1. Approximate spatial distribution ahead of a Mode I sharp stationary crack of the tensile stress across the crack plane for 2219-T851 at 175°C (log scales). The variations of the singular terms only are shown (See Table I-1 for a list of the data used in the calculations).

Figure 2. Sketch of the CT specimens used in this study. The specimens were machined with either 40% side grooves (.25 cm = 1" deep), 20% side grooves (.13 cm = .05" deep), or 0% side grooves.

Figure 3. Comparison between the experimental compliance calibration for CT specimens with 40% side grooves and the empirical compliance calibrations reported in Reference [36] for side grooved specimens under plane stress and plane strain conditions.

Figure 4. Effect of hold time on crack growth rates per cycle (Note: K = maximum stress intensity factor, h.t. = hold time and l.t. = loading (or unloading) time).

Figure 5. Effect of hold time on crack growth rates per unit time for $\frac{da}{dt}$ = cycle frequency x $\frac{da}{dN}$.
(Note: The scatter band shown in the following graphs corresponds to the scatter in this figure.)

Figure 6. Typical log-log crack growth curve.

Figure 7. Effect of side grooves depth on crack growth rates per unit time.

Figure 8. Effect of the initial stress intensity factor on crack growth rates per unit time.

Figure 9. (a) Variations of K_{max} as a function of a/w for constant K_{max} tests.
(b) Variations of da/dt as a function of a/w for constant K_{max} tests.

Figure 10. Effect of temperature on crack growth rates per unit time.

Figure 11. Effect of cycle frequency for cycles with no hold time on crack growth rates per cycle. The effect of a hold time at maximum load is also clearly demonstrated.

Figure 12. Effect of cycle frequency and hold time on crack growth rates per cycle.

Figure 13. SEM Fractograph of a CCG specimen showing the fracture features corresponding to low crack growth rates ($K_{max} \lesssim 20$ MPa$\sqrt{m}$) (X500 and X1000).

Figure 14. SEM Fractograph of a CCG specimen showing the fracture features corresponding to higher crack growth rates ($K_{max} \gtrsim 25$ MPa$\sqrt{m}$) (X500 and X1000).

Figure 15. SEM Fractograph of a FCG specimen showing the fracture features corresponding to low cycle frequencies ($\nu \lesssim 0.1$ Hz) (X500 and X1000).

Figure 16. SEM Fractograph of an FCG specimen showing the fracture features corresponding to higher cycle frequencies ($\nu \gtrsim 1$ Hz) (X500 and X1000).

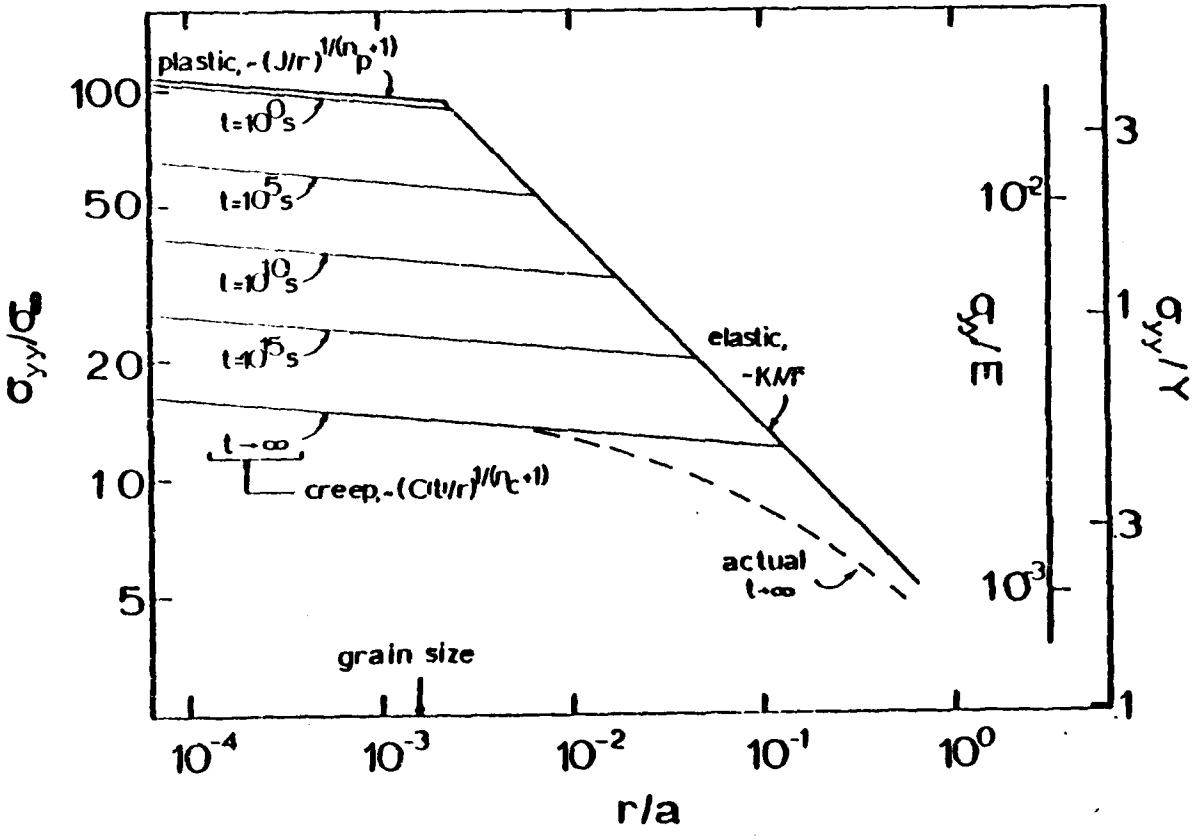

FIGURE 1 Approximate spatial distribution ahead of a Mode I sharp stationary crack of the tensile stress across the crack plane for 2219-T851 at 175°C (log scales). The variations of the singular terms only are shown (See Table (I-1) for a list of the data used in the calculations).

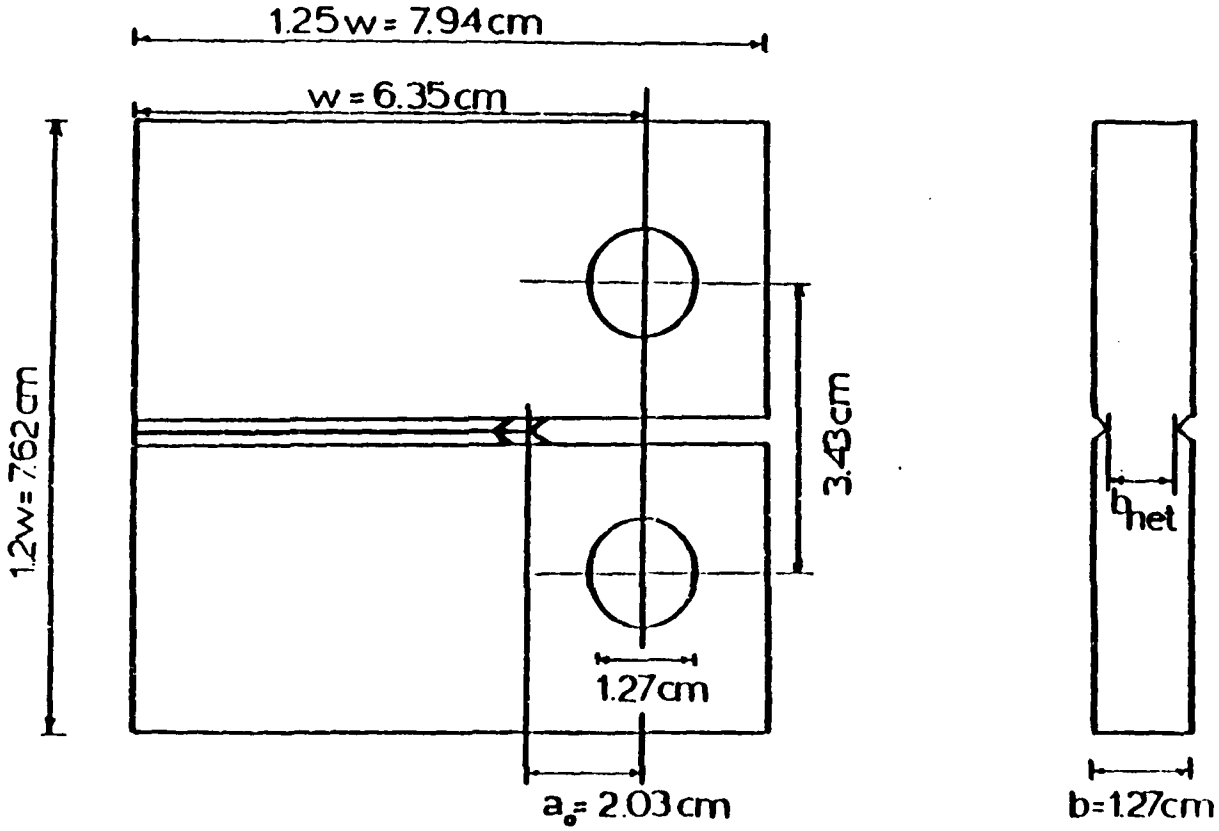

FIGURE 2 Sketch of the CT specimens used in this study. The specimens were machined with either 40% side grooves (.25 cm = .1" deep), 20% (.13 cm = .05" deep) side grooves, or 0% side grooves.

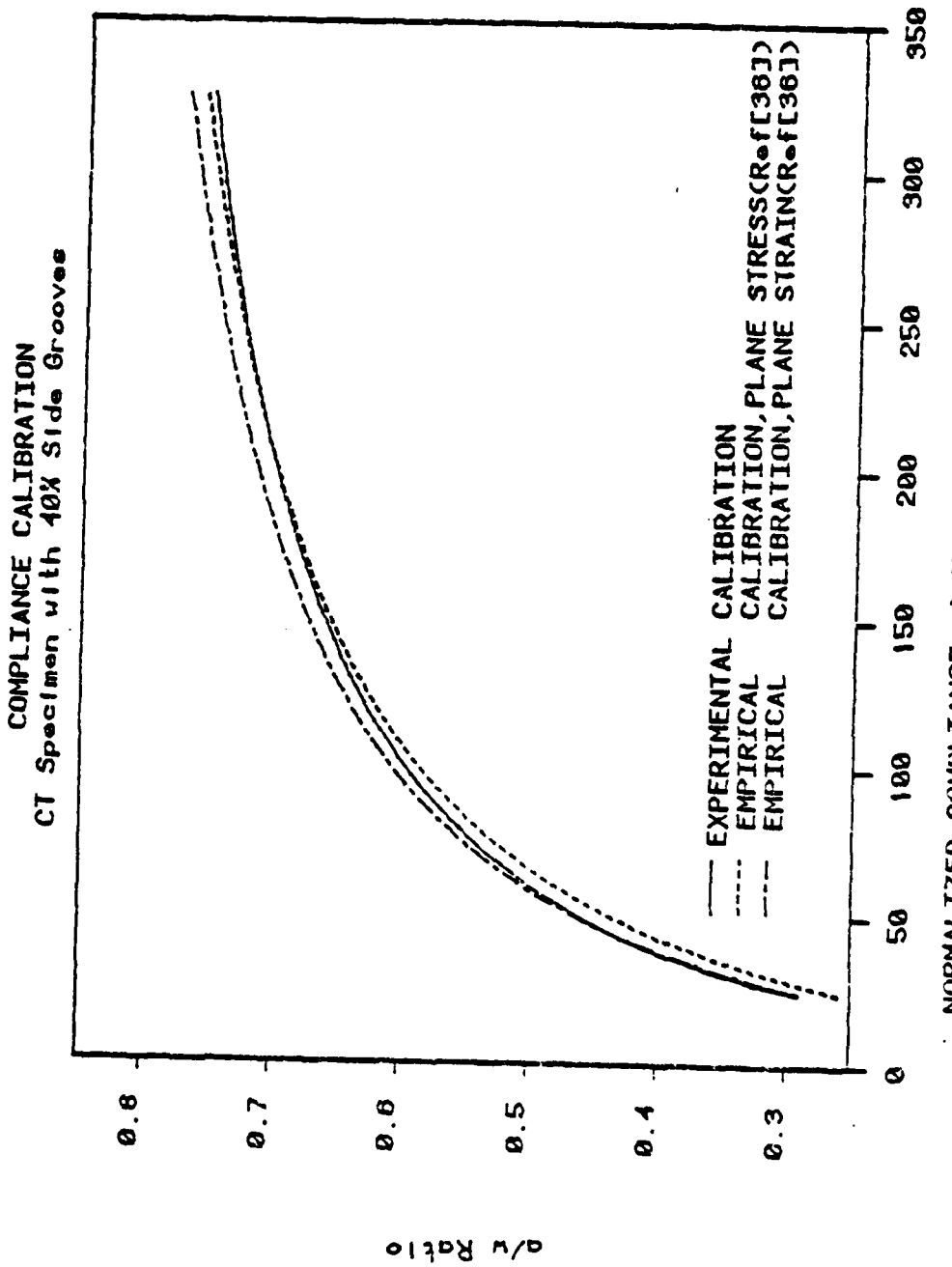

FIGURE 3 Comparison between the experimental compliance calibration for CT specimens with 40% side grooves and the empirical compliance calibrations reported in Reference [36] for side grooved specimens under plane stress and plane strain conditions.

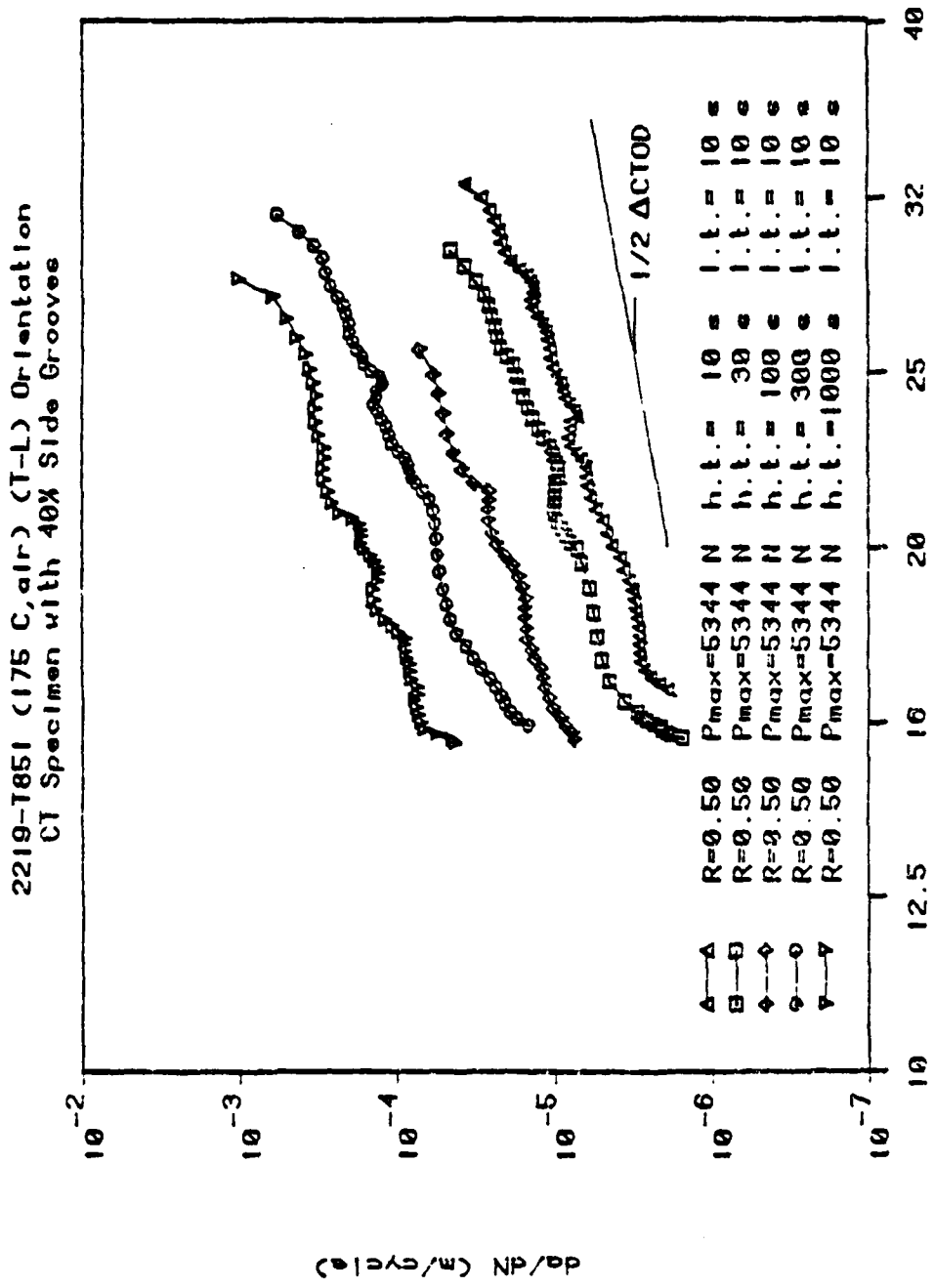

FIGURE 4 Effect of hold time on crack growth rates per cycle (Note: K = maximum stress intensity factor, h.t. = hold time and l.t. = loading (or unloading) time).

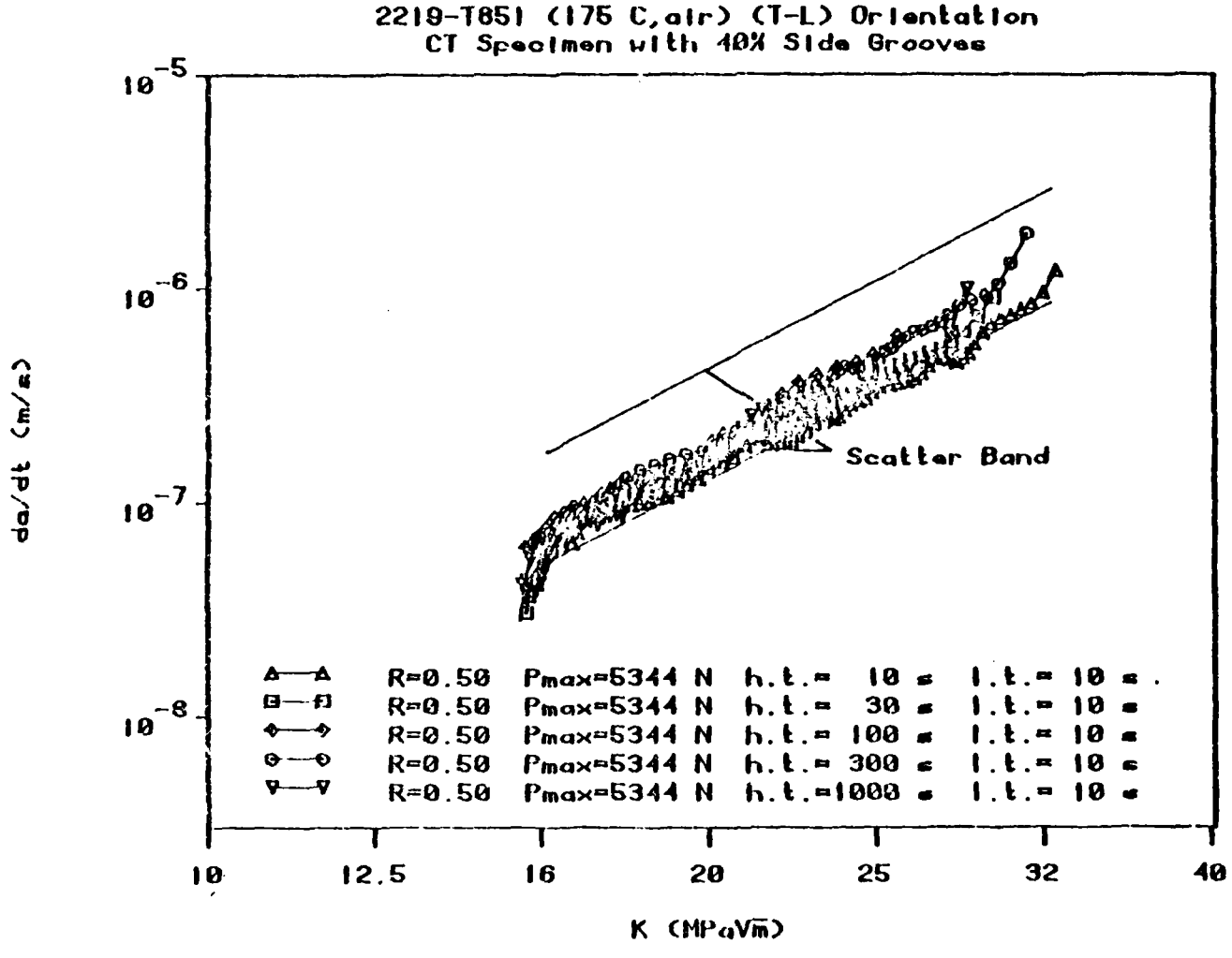

FIGURE 5 Effect of hold time on crack growth rates per unit time for $\frac{da}{dt}$ = cycle frequency x $\frac{da}{dN}$.

(Note: The scatter band shown in the following graphs corresponds

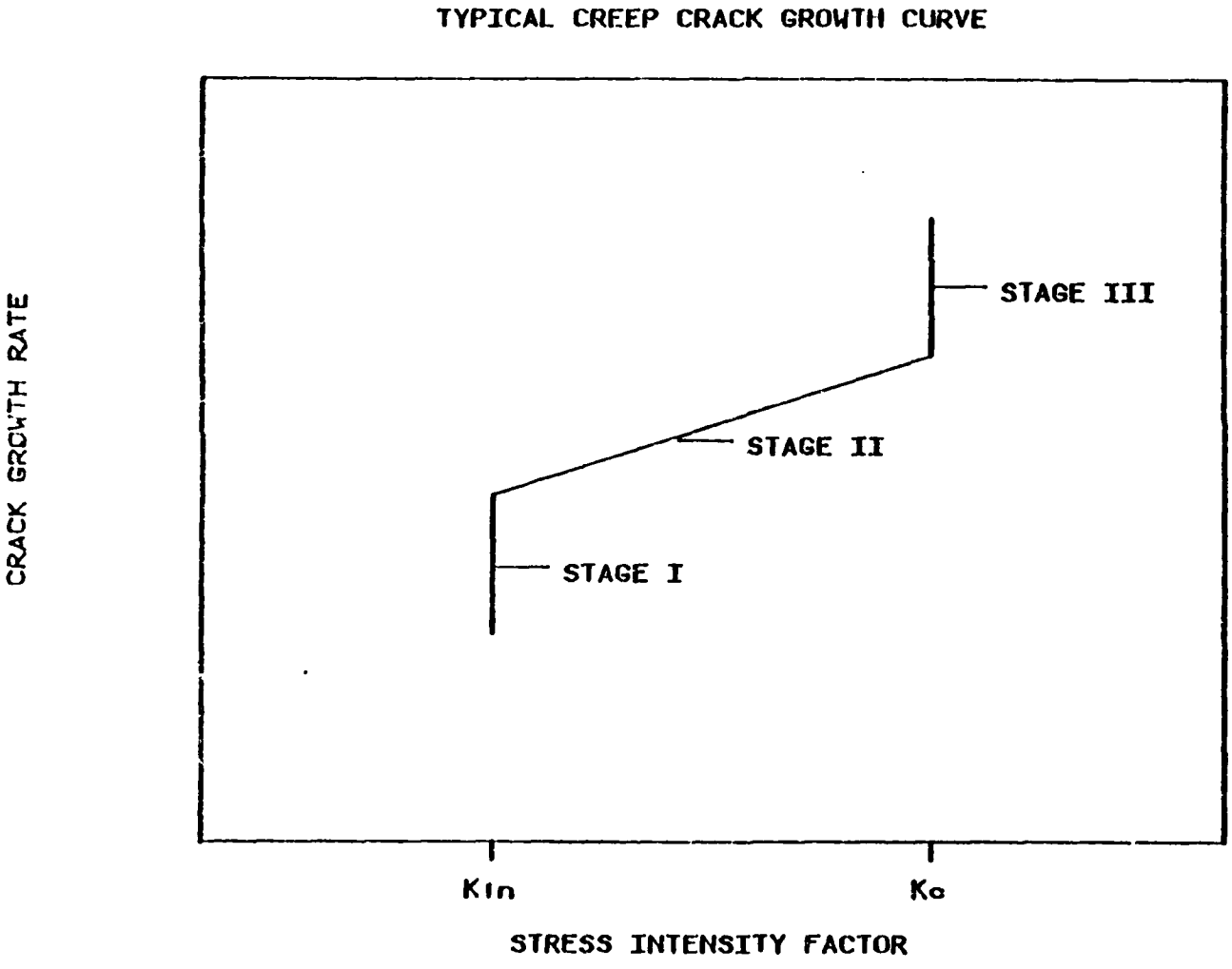

FIGURE 6 Typical log-log crack growth curve.

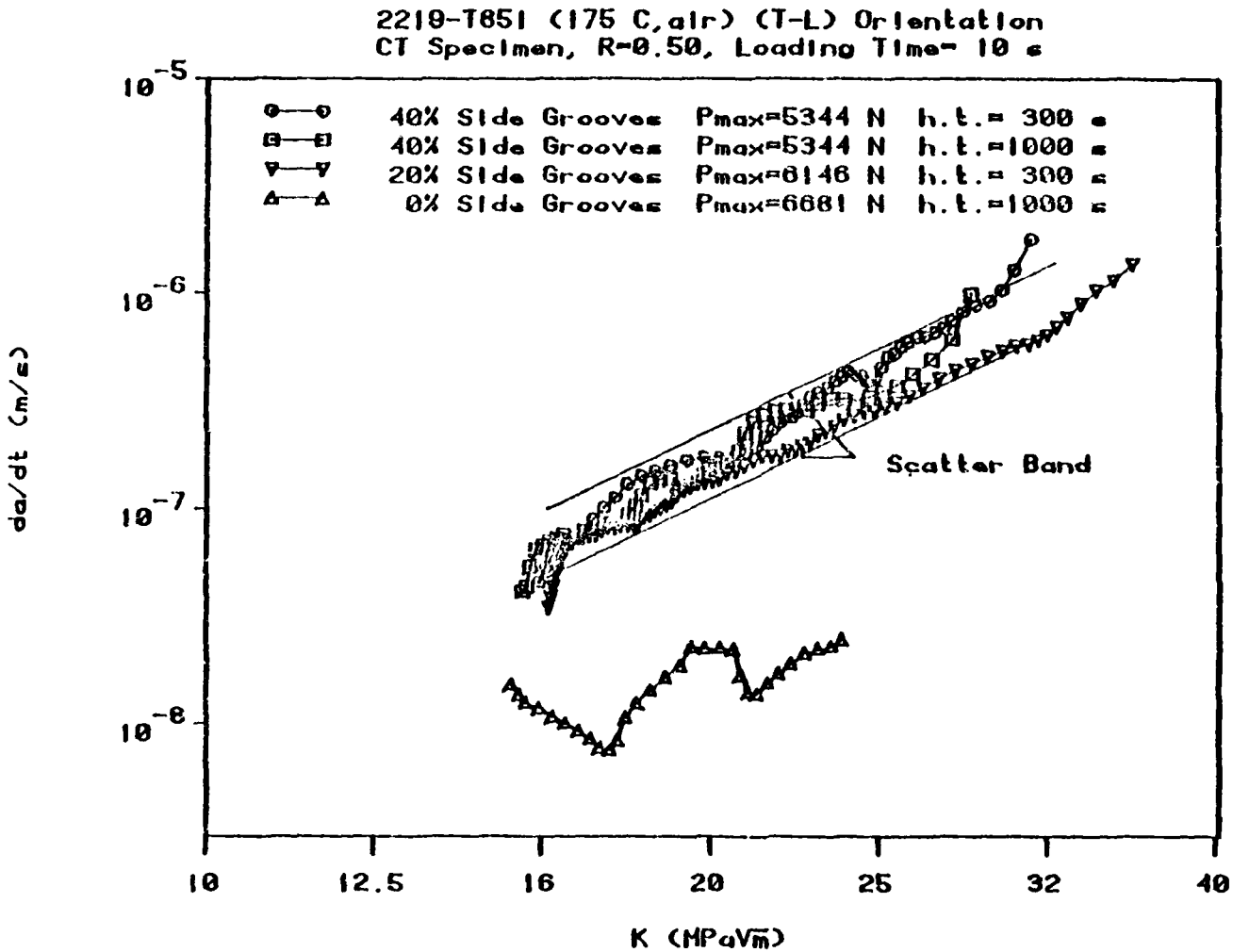

FIGURE 7 Effect of side grooves depth on crack growth rates per unit time.

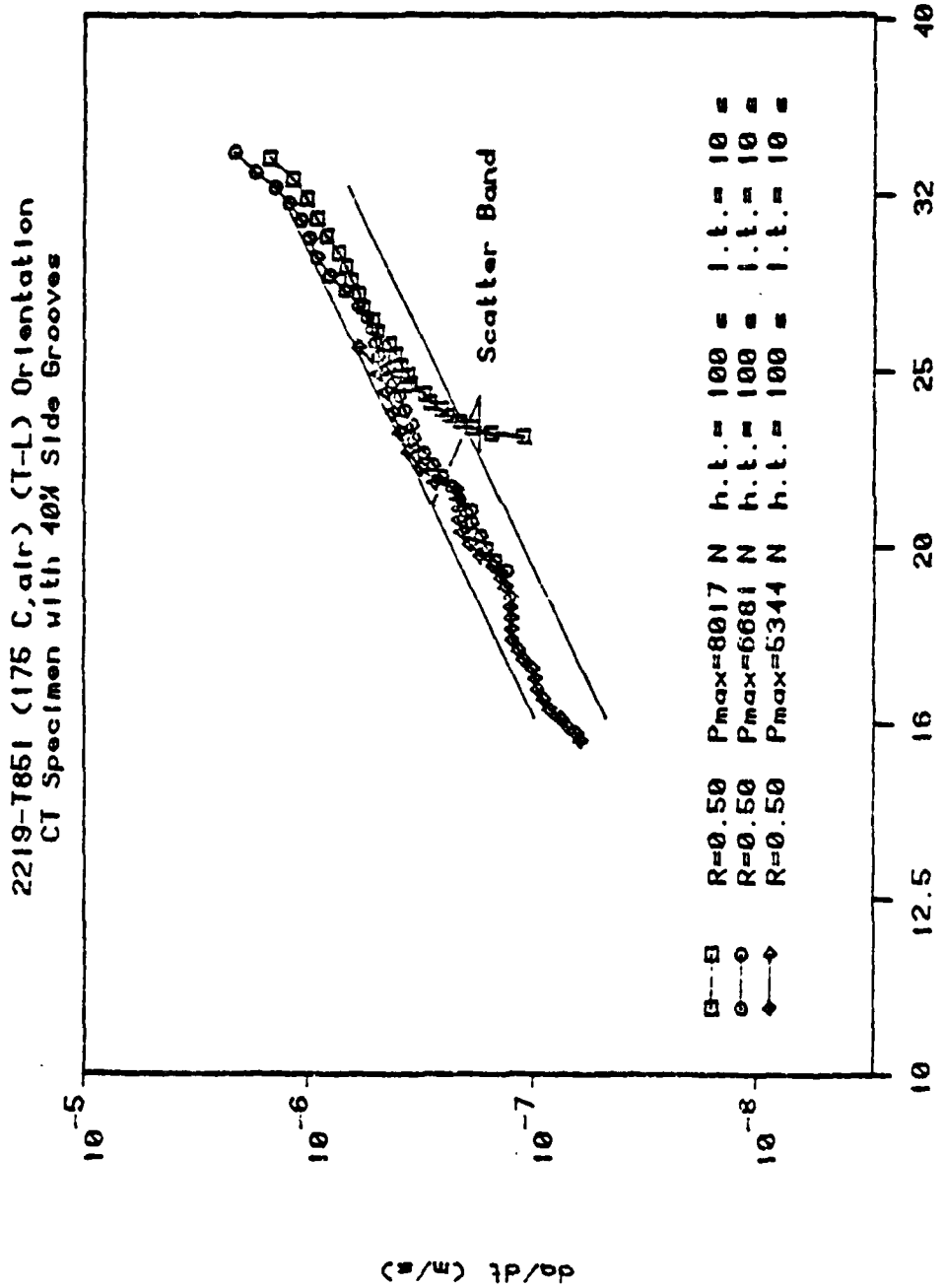

FIGURE 8 Effect of the initial stress intensity factor on crack growth rates per unit time.

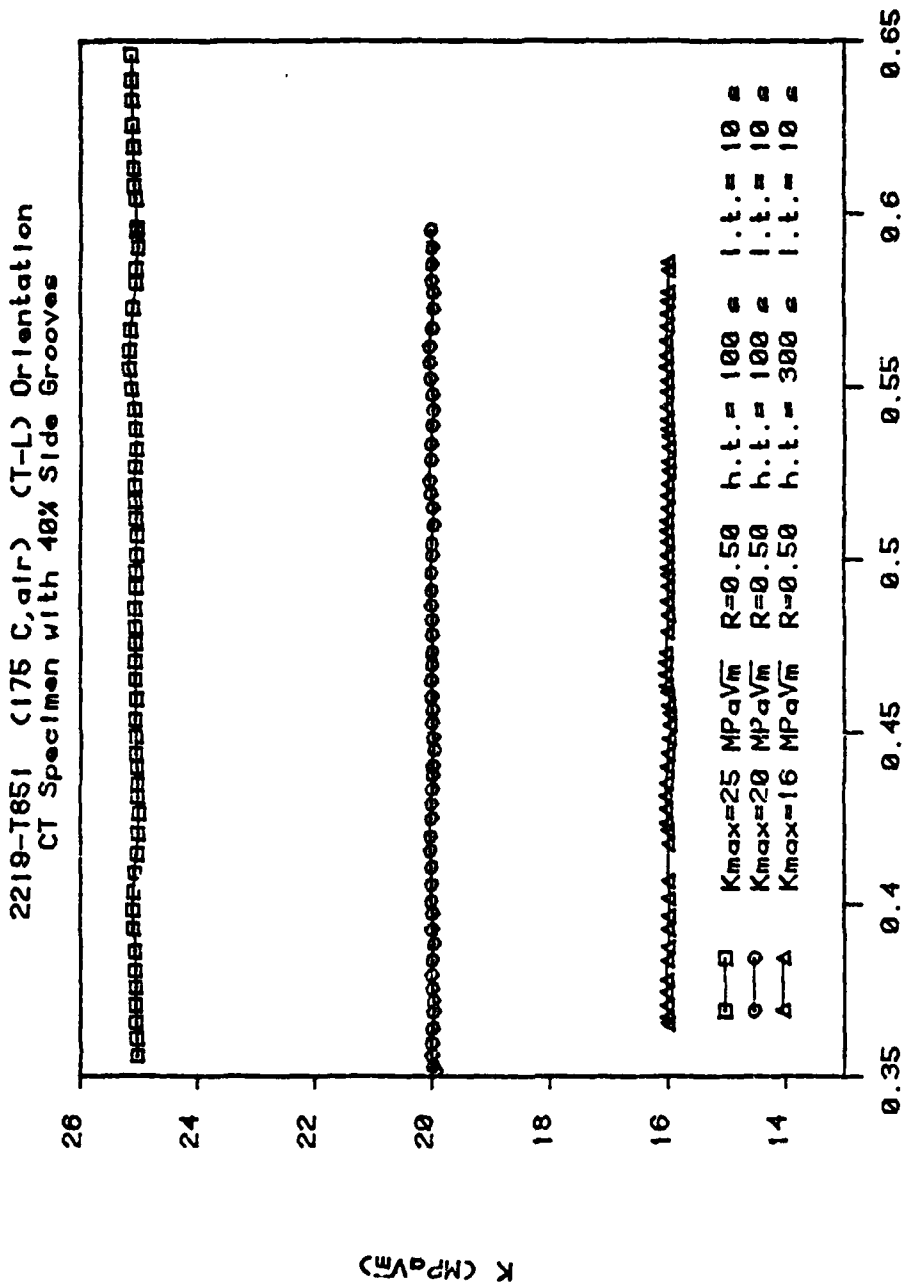

FIGURE 9a Variations of K_{max} as a function of a/w for a typical constant K_{max} test

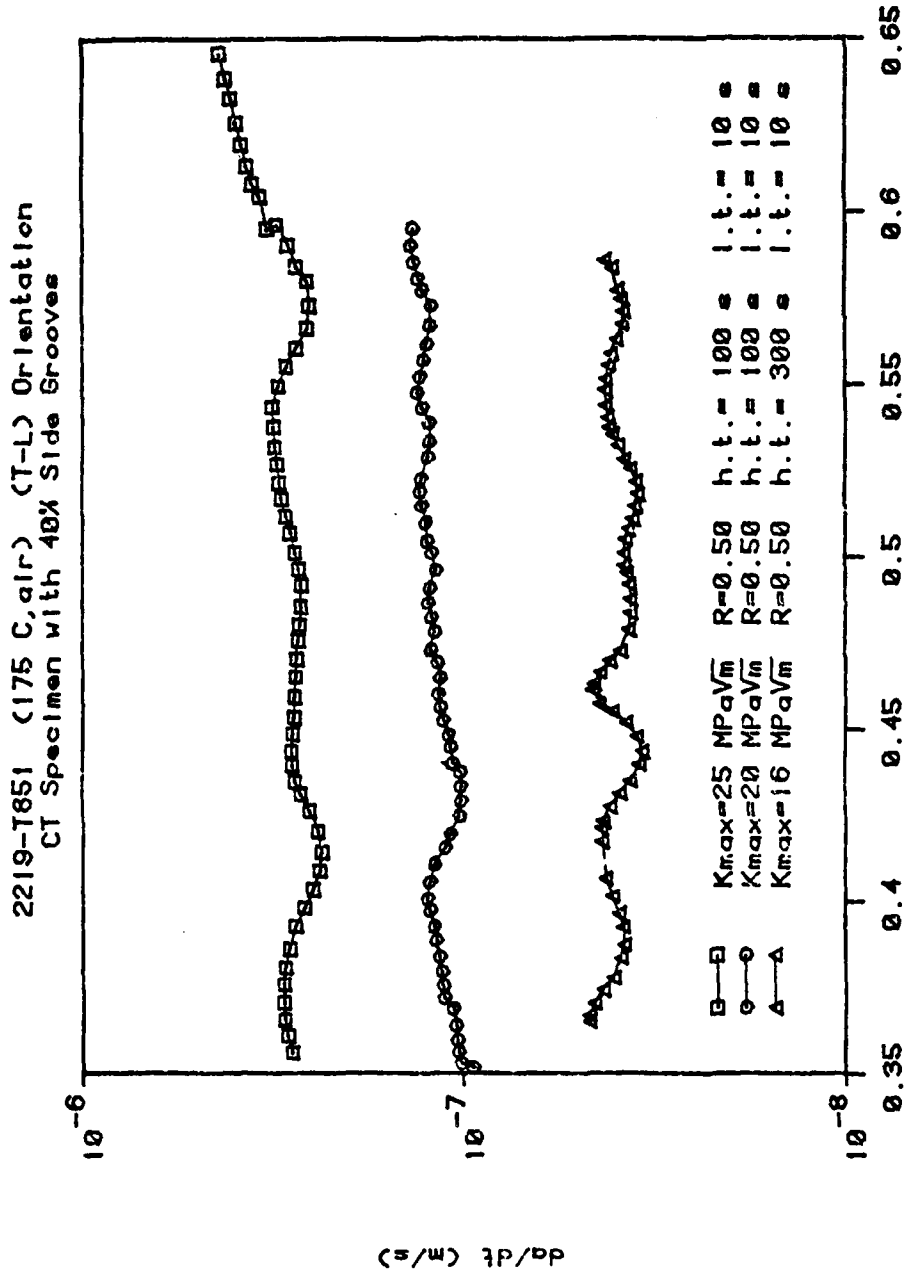

FIGURE 9b Variations of da/dt as a function of a/w for a typical constant Kmax test

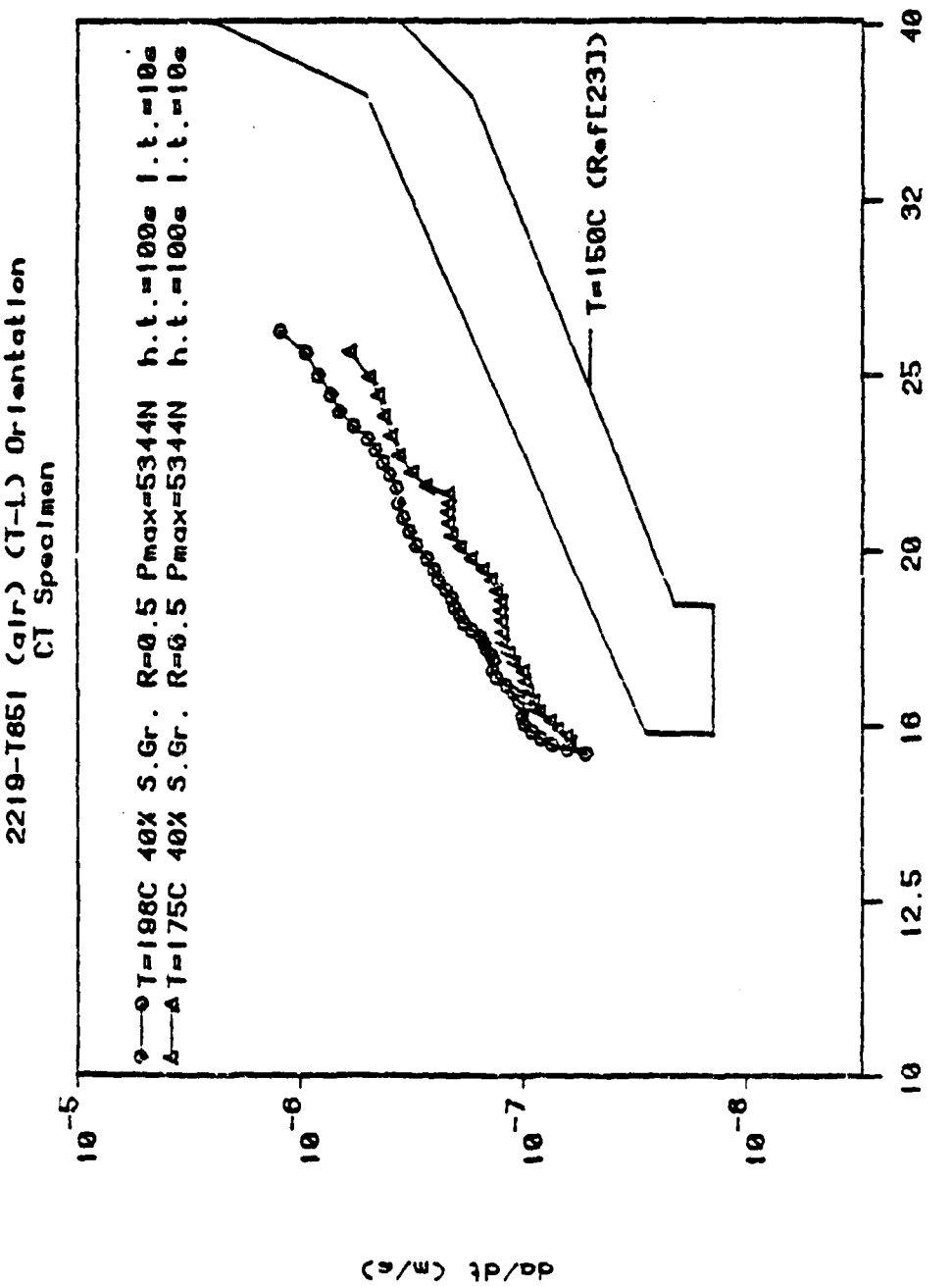

FIGURE 10 Effect of temperature on crack growth rates per unit time.

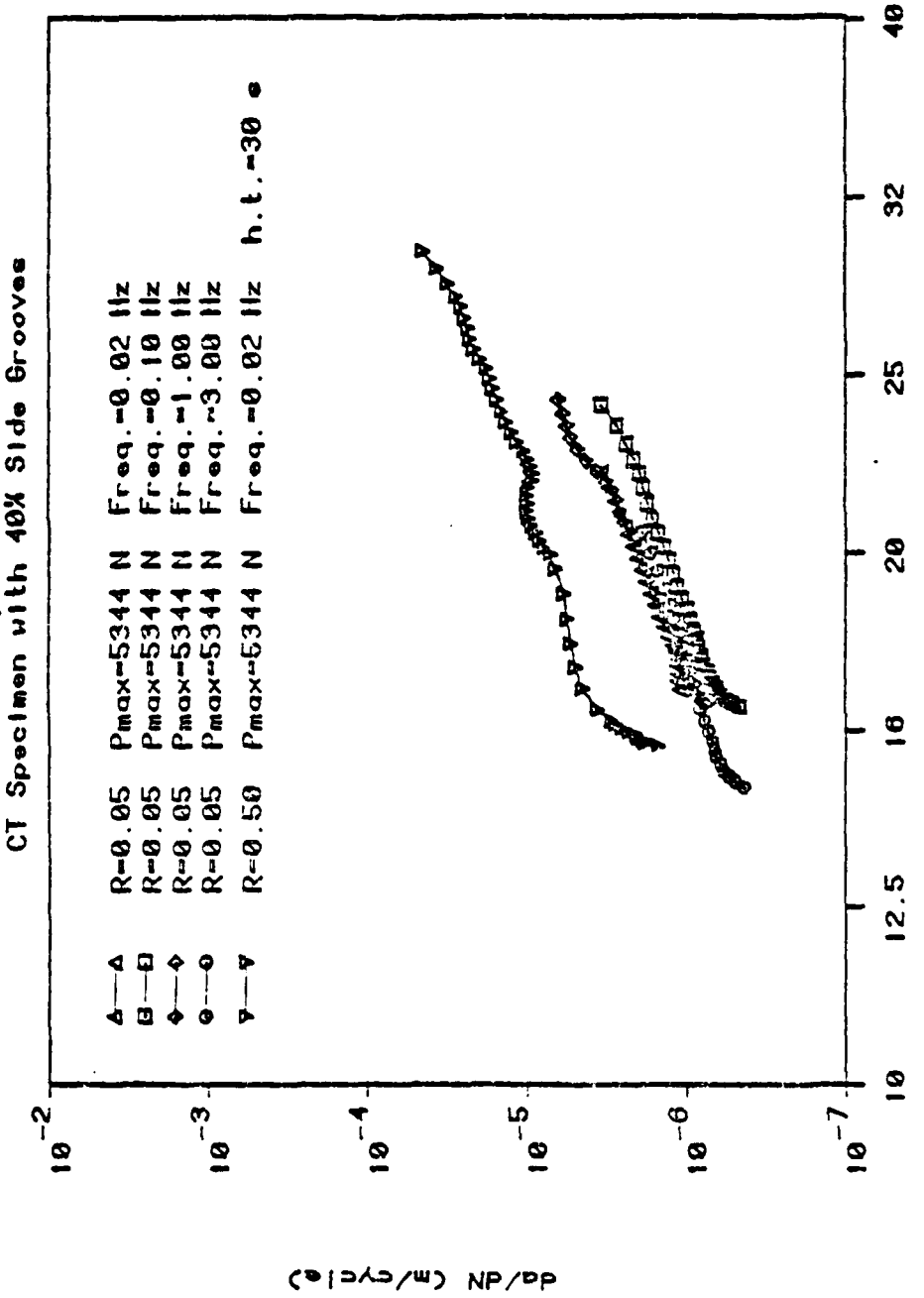

FIGURE 11 Effect of cycle frequency for cycles with no hold time on crack growth rates per cycle. The effect of a hold time at maximum load is also clearly demonstrated.

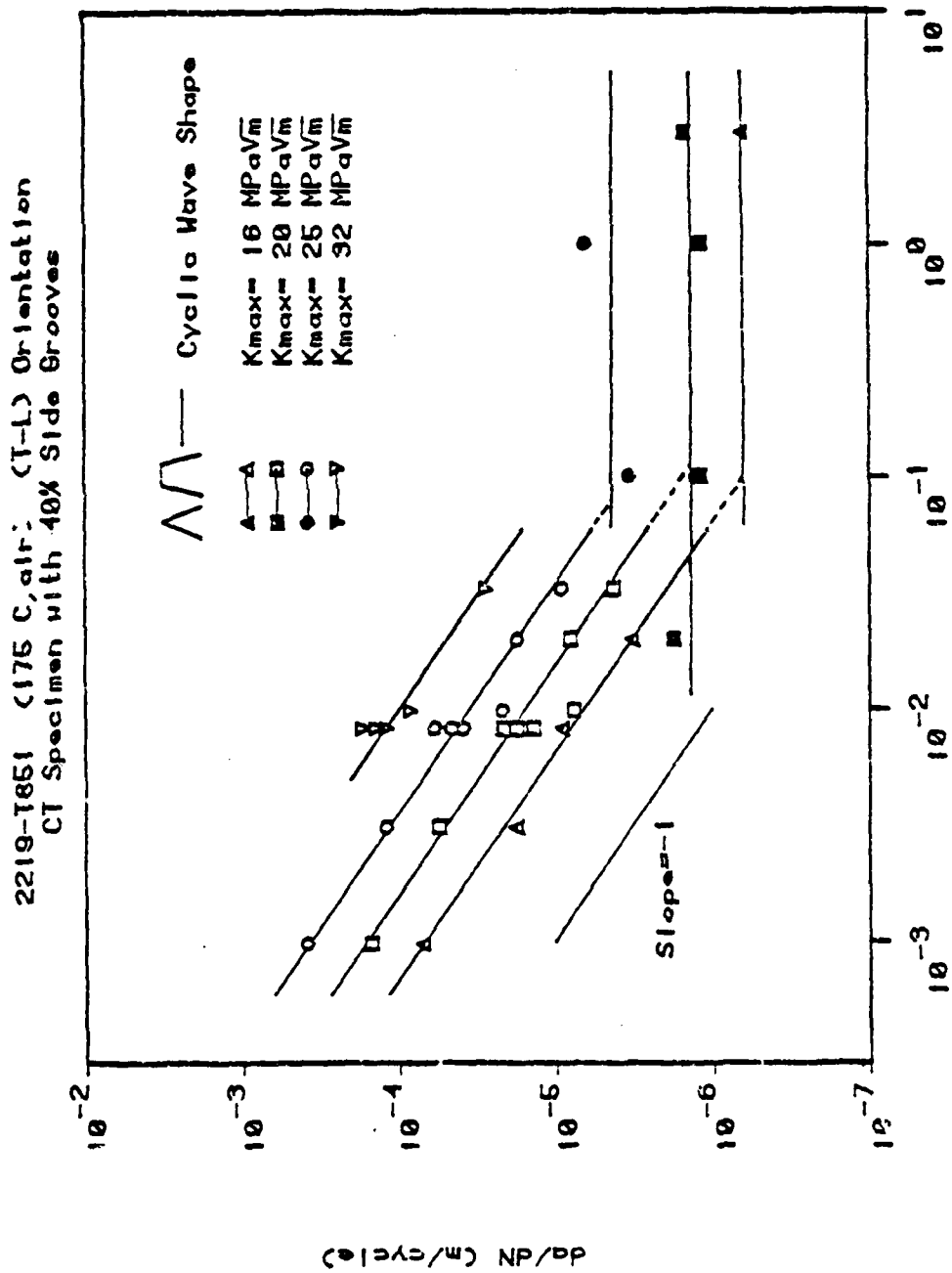

FIGURE 12 Effect of cycle frequency and hold time on crack growth rates per cycle.

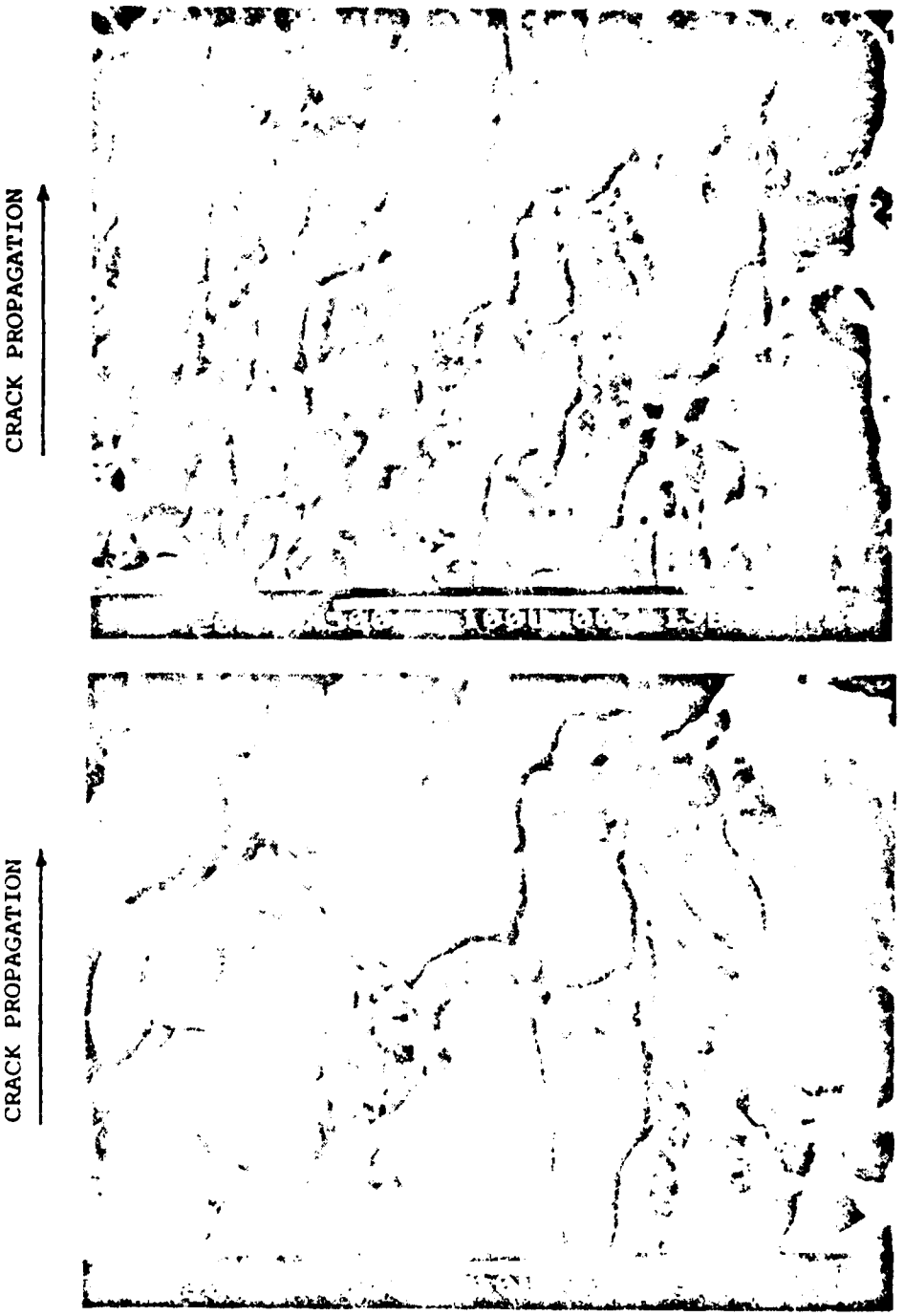

FIGURE 13 SEM Fractograph of a CCG specimen showing the fracture features corresponding to low crack growth rates ($K_{max} \leq 20$ MPa$\sqrt{m}$) (X500 and X1000).

Copy available to DTIC does not permit fully legible reproduction

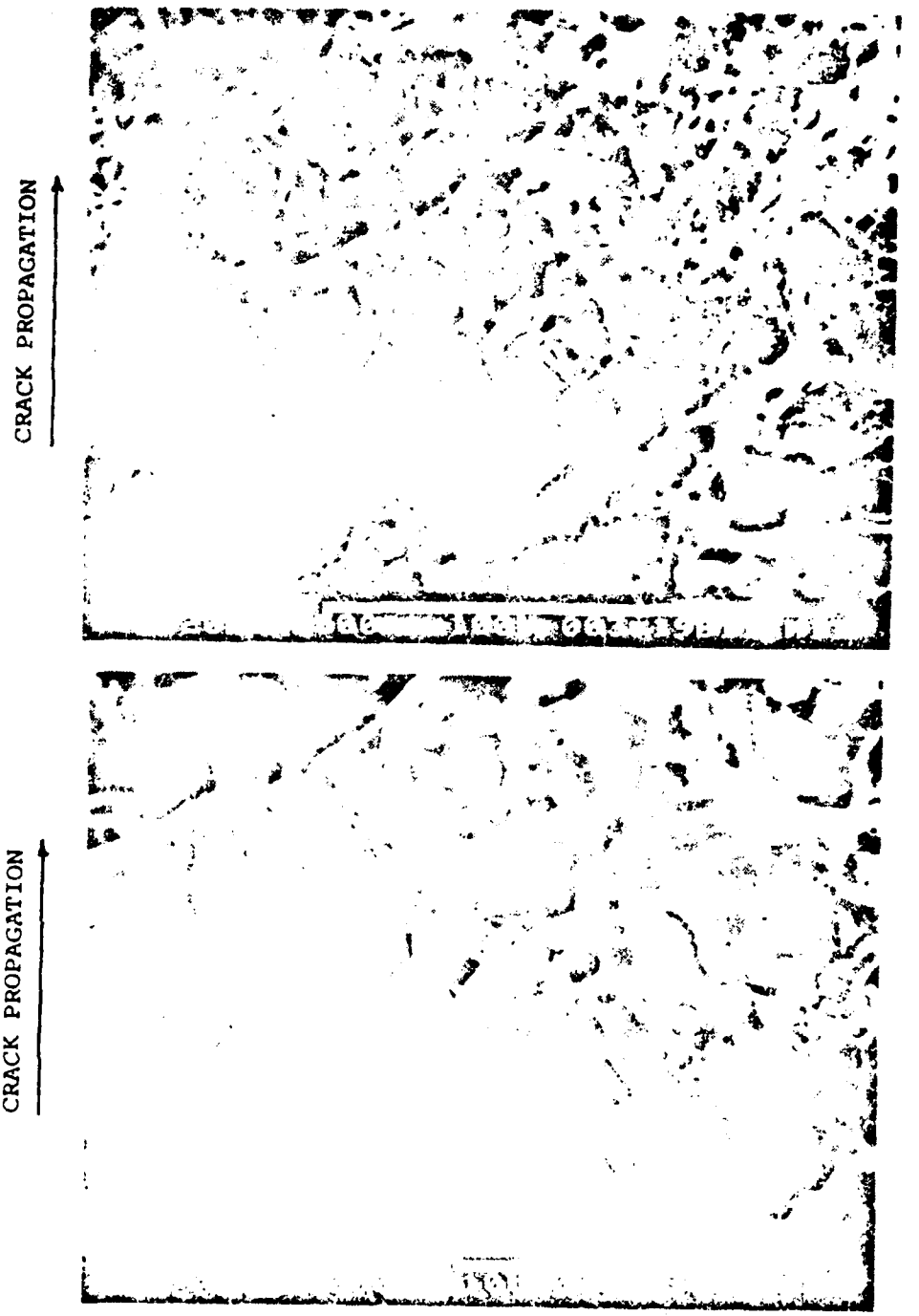

FIGURE 14 SEM Fractograph of a CCG specimen showing the fracture features corresponding to higher crack growth rates ($K_{max} \geq$ 25 MPa$\sqrt{m}$) (X500 and X1000).

Copy available to DTIC does not permit fully legible reproduction

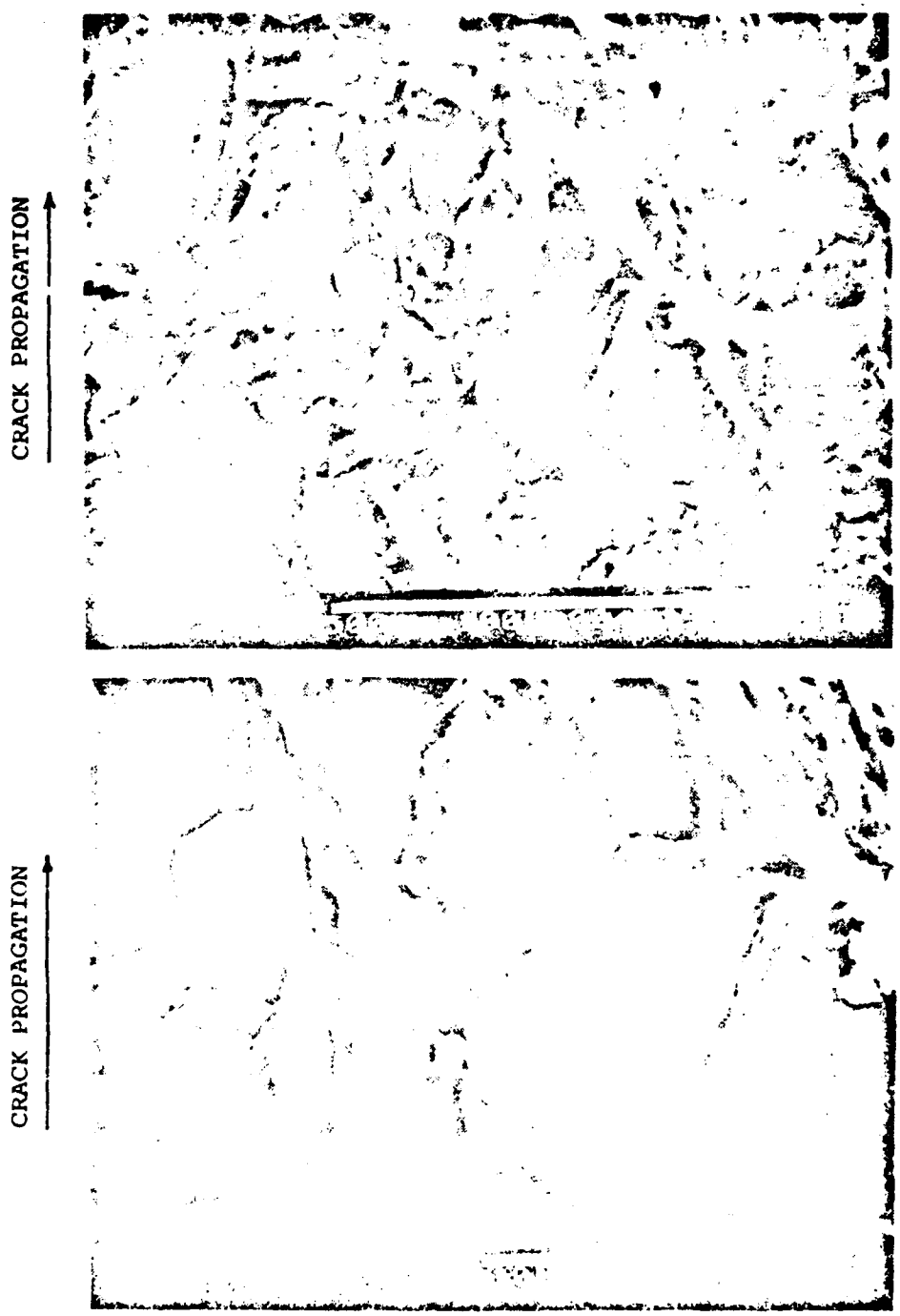

FIGURE 15 SEM Fractograph of a FCG specimen showing the fracture features corresponding to low cycle frequencies ($\nu \leq 0.1$ Hz) (X500 and X1000).

Copy available to DTIC does not permit fully legible reproduction

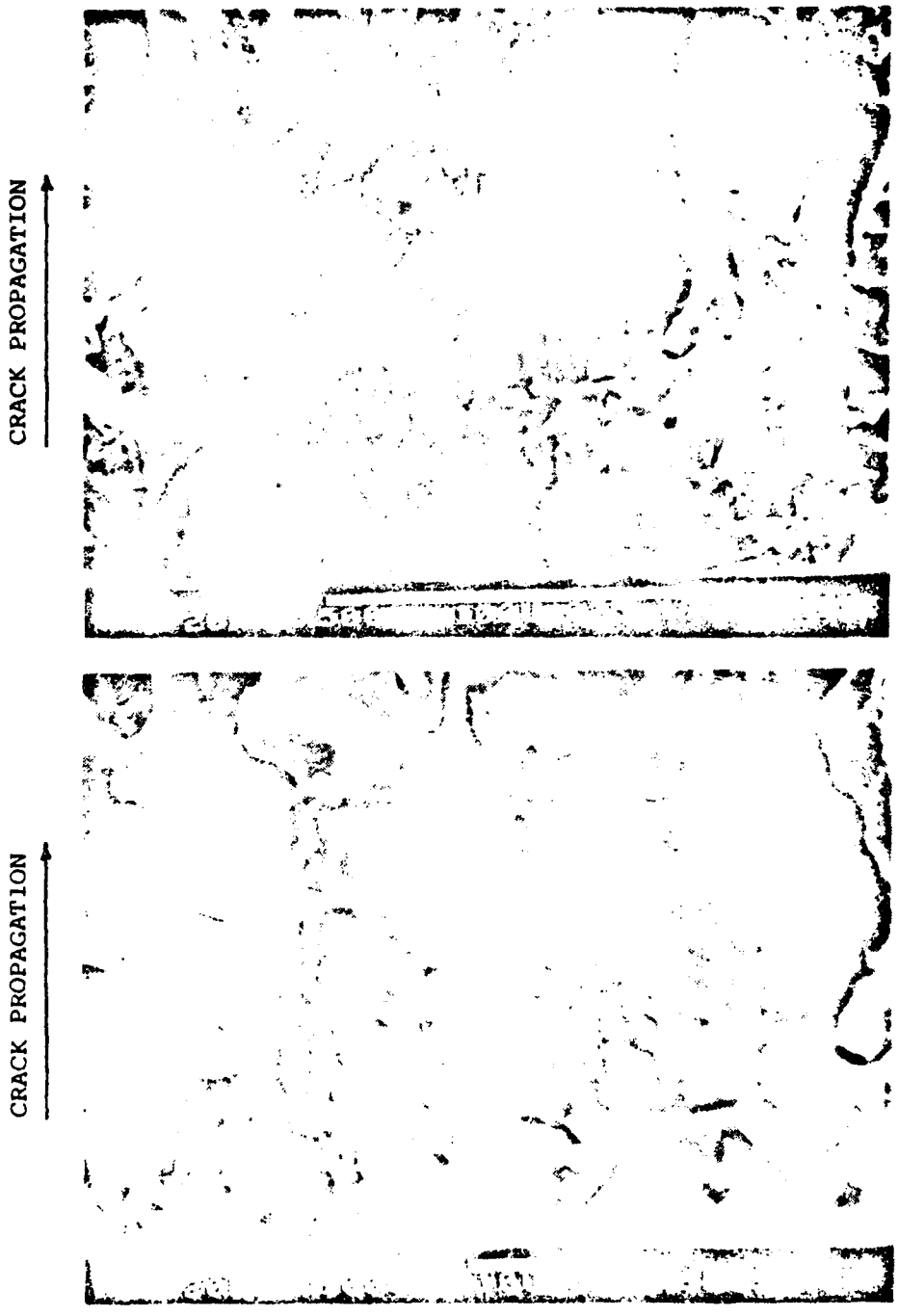

FIGURE 16 SEM Fractograph of an FCG specimen showing the fracture features corresponding to higher cycle frequencies ($\nu \geq 1$ Hz) X500 and X1000

Copy available to DTIC does not permit fully legible reproduction

APPENDIX 1

COMPLIANCE CALIBRATION AT THE LOCATION OF KNIFE EDGES FOR SMOOTH CT SPECIMENS

For CT specimens with no side grooves, the loading line normalized compliance $\left(Eb\,\frac{\Delta v}{\Delta P}\right)_{LL}$ is given by ([35]):

$$\left(Eb\,\frac{\Delta v}{\Delta P}\right)_{LL} = \left(\frac{1 + a/w}{1 - a/w}\right)^2 \left(2.1630 + 12.219\,\frac{a}{w} - 20.065\left(\frac{a}{w}\right)^2 - 0.9925\left(\frac{a}{w}\right)^3 + 20.609\left(\frac{a}{w}\right)^4 - 9.9314\left(\frac{a}{w}\right)^5\right) \tag{A1-1}$$

The normalized compliance at the location of the knife edges $\left(Eb\,\frac{\Delta v}{\Delta P}\right)$ is given by:

$$\left(Eb\,\frac{\Delta v}{\Delta P}\right) = \left(\frac{x_0/w + 0.27}{x_0/w}\right)\left(Eb\,\frac{\Delta v}{\Delta P}\right)_{LL} \tag{A1-2}$$

where x_0/w is the normalized location of the axis of rotation of the arms of the specimen given by ([35]):

$$\frac{x_0}{w} = -0.0995314 + 3.02437\,\frac{a}{w} - 7.95768\left(\frac{a}{w}\right)^2 + 13.546\left(\frac{a}{w}\right)^3 - 10.6274\left(\frac{a}{w}\right)^4 + 3.1133\left(\frac{a}{w}\right)^5 \tag{A1-3}$$

A least square fit of a/w as a function of $\left(Eb\,\frac{\Delta v}{\Delta P}\right)$ yields then:

$$\frac{a}{w} = 1.025 - 6.07807\,U + 47.1092\,U^2 - 509.145\,U^3 + 2417.19\,U^4 - 4064.67\,U^5 \tag{A1-4}$$

where U is defined by:

$$U = 1\Big/\left(\left(E'b\,\frac{\Delta v}{\Delta P}\right)^{1/2} + 1\right) \tag{II-4a}$$

with

$E' = E$ under plane stress conditions (II-4b)

$E' = \frac{E}{1 - \nu^2}$ under plane strain conditions. (II-4c)

APPENDIX 2

STRESS INTENSITY FOR SPECIMENS WITH SIDE GROOVES

Since the loading line compliance $\left(Eb\,\frac{\Delta v}{\Delta P}\right)_{LL}$ is almost not modified by the presence of side grooves, one can write ([16]):

$$G_{\text{no side grooves}} = \frac{P^2}{2b}\,\frac{1}{Ebw}\,\frac{\partial\left(Eb\,\frac{\Delta v}{\Delta P}\right)_{LL}}{\partial\left(\frac{a}{w}\right)} \qquad \text{(A2-1)}$$

$$G_{\text{side grooves}} = \frac{P^2}{2b_{net}}\,\frac{1}{Ebw}\,\frac{\partial\left(Eb\,\frac{\Delta v}{\Delta P}\right)_{LL}}{\partial\left(\frac{a}{w}\right)} \qquad \text{(A2-2)}$$

Thus: $G_{\text{side grooves}} \cong G_{\text{no side grooves}}\left(\frac{b}{b_{net}}\right)$

Since $K = \sqrt{EG}$, finally:

$$K_{\text{side grooves}} \cong \sqrt{\frac{b}{b_{net}}}\;K_{\text{no side grooves}} \qquad \text{(A2-3)}$$

By using (A2-3) and (II-6), (II-7) follows.

APPENDIX 3

EXPERIMENTAL STRESS INTENSITY FACTOR FOR SPECIMENS WITH 40% SIDE GROOVES

Assuming that the location (x_0/w) of the axis of rotation of the arms of the specimen is not affected by the presence of side grooves, the loading line compliance for CT specimens with 40% side grooves is given by:

$$\left(bE\,\frac{\Delta v}{\Delta P}\right)_{LL} = \left(\frac{x_0/w}{x_0/w + .27}\right) \cdot \left(bE\,\frac{\Delta v}{\Delta P}\right) \qquad \text{(A3-1)}$$

where x_0/w is given by (A1-3) as a function of a/w, a/w being obtained from (II-1):

$$x_0/w = -0.0995314 + 3.02437\,\frac{a}{w} - 7.95768\left(\frac{a}{w}\right)^2 + 13.546\left(\frac{a}{w}\right)^3 - 10.6274\left(\frac{a}{w}\right)^4 + 3.1133\left(\frac{a}{w}\right)^5 \qquad \text{(A1-3)}$$

$$\frac{a}{w} = .943769 - 4.29331\,U + 38.0499\,U^2 - 698.674\,U^3 + 4721.32\,U^4 - 10886.8\,U^5 \qquad \text{(II-1)}$$

with $U = 1\Big/\left(\left(Eb\,\frac{\Delta v}{\Delta P}\right)^{1/2} + 1\right)$, $\left(Eb\,\frac{\Delta v}{\Delta P}\right)$ being the compliance at the location of the knife edges.

A least square fit resulted in:

$$\left(Eb\,\frac{\Delta v}{\Delta P}\right)_{LL} = \left(\frac{1 + a/w}{1 - a/w}\right)^2 \left(5.47027 - 4.6455\,\frac{a}{w} - 23.0476\left(\frac{a}{w}\right)^2 + 152.81\left(\frac{a}{w}\right)^3 - 268.902\left(\frac{a}{w}\right)^4 + 153.152\left(\frac{a}{w}\right)^5\right) \qquad \text{(A3-2)}$$

According to (A2-2) and (A2-3):

$$K_{exp} = \frac{P}{\sqrt{b}\,B_{net}\,w}\left(\frac{1}{2}\,\frac{\partial\,(Eb\,\Delta v/\Delta P)_{LL}}{\partial\,(a/w)}\right)^{1/2} \qquad \text{(A3-3)}$$

or, by a least square fit:

$$K_{exp} = \frac{P}{\sqrt{b}\,B_{net}\,w}\,\frac{(2 + a/w)}{(1 - a/w)^{3/2}}\left(.374907 + 6.52948\,\frac{a}{w} - 10.5935\left(\frac{a}{w}\right)^2 + .703939\left(\frac{a}{w}\right)^3 + 5.28039\left(\frac{a}{w}\right)^4\right) \qquad \text{which is (II-8).} \qquad \text{(A3-4)}$$

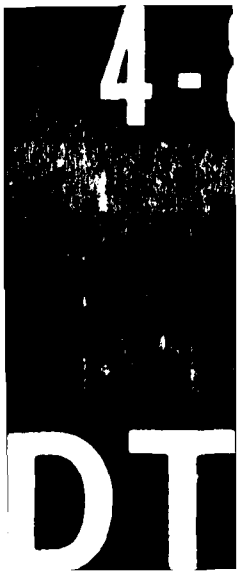
4-
DT